DEVELOPMENT OF AN EXPERIMENTALLY VERIFIED HIGH-FIDELITY MODEL OF A QUARTZ FLEXIBLE ACCELEROMETER

A THESIS SUBMITTED TO
THE GRADUATE SCHOOL OF NATURAL and APPLIED SCIENCES
OF
MIDDLE EAST TECHNICAL UNIVERSITY

BY

HASAN BARAN ÖZMEN

IN PARTIAL FULFILLMENT OF THE REQUIREMENTS
FOR
THE DEGREE OF MASTER OF SCIENCE
IN
AEROSPACE ENGINEERING

JANUARY 2024

Approval of the thesis:

DEVELOPMENT OF AN EXPERIMENTALLY VERIFIED HIGH-FIDELITY MODEL OF A QUARTZ FLEXIBLE ACCELEROMETER

submitted by **HASAN BARAN ÖZMEN** in partial fulfillment of the requirements for the degree of **Master of Science** i**n Aerospace Engineering, Middle East Technical University** by,

Prof. Dr. Halil Kalıpçılar
Dean, Graduate School of **Natural and Applied Sciences** _____

Prof. Dr. Serkan Özgen
Head of the Department, **Aerospace Engineering** _____

Assoc. Prof. Dr. Melin Şahin
Supervisor, **Aerospace Engineering, METU** _____

Assist. Prof. Dr. Gökhan O. Özgen
Co-Supervisor, **Mechanical Engineering, METU** _____

Examining Committee Members:

Prof. Dr. Ozan Tekinalp
Aerospace Engineering, METU _____

Assoc. Prof. Dr. Melin Şahin
Aerospace Engineering, METU _____

Prof. Dr. Ender Ciğeroğlu
Mechanical Engineering, METU _____

Assist. Prof. Dr. Gökhan O. Özgen
Mechanical Engineering, METU _____

Assist. Prof Dr. Kutluk Bilge Arıkan
Mechanical Engineering, TEDU _____

Date: 26.01.2024

I hereby declare that all information in this document has been obtained and presented in accordance with academic rules and ethical conduct. I also declare that, as required by these rules and conduct, I have fully cited and referenced all material and results that are not original to this work.

Name Last name : Hasan Baran Özmen

Signature :

ABSTRACT

DEVELOPMENT OF AN EXPERIMENTALLY VERIFIED HIGH-FIDELITY MODEL OF A QUARTZ FLEXIBLE ACCELEROMETER

Özmen, Hasan Baran
Master of Science, Aerospace Engineering
Supervisor: Assoc. Prof. Dr. Melin Şahin
Co-Supervisor: Assist. Prof. Dr. Gökhan O. Özgen

January 2024, 82 pages

Quartz Flexible Accelerometers (QFA) are one of the most commonly utilized accelerometer types within tactical and navigational grade inertial navigation systems, owing to their low noise, long-term stability and dynamic performance characteristics. This thesis focuses on the development and validation of a comprehensive mathematical model for the QFA, aiming to enhance the understanding and dynamic performance evaluation of this sensor type. The study involves modelling of the accelerometer both as an open loop system and closed loop system. Subsequently, the proposed models are experimentally verified through tests with open and closed loop test prototypes. The experimental results confirm the accuracy and reliability of the developed model, demonstrating its capability to predict the sensor's dynamic behavior in real-world scenarios. The closed loop model is then used to investigate the effects of various design parameters on dynamic performance. Finally, this experimentally validated closed loop system is expected to serve as a high-fidelity model for further optimization and design improvement studies on the QFAs.

Keywords: Quartz Flexible Accelerometer, Inertial Sensor, Closed Loop System Modelling, Experimental Verification, High-Fidelity Model

ÖZ

KUVARS SARKAÇLI BİR İVMEÖLÇERİN DENEYSEL OLARAK DOĞRULANMIŞ YÜKSEK SADAKATLİ MODELİNİN GELİŞTİRİLMESİ

Özmen, Hasan Baran
Yüksek Lisans, Havacılık ve Uzay Mühendisliği
Tez Yöneticisi: Doç. Dr. Melin Şahin
Ortak Tez Yöneticisi: Dr. Öğr. Üyesi Gökhan O. Özgen

Ocak 2024, 82 sayfa

Kuvars Sarkaçlı İvmeölçerler (KSİ) düşük gürültü, uzun dönem kararlılık ve dinamik performans özellikleri ile taktik ve navigasyon seviye ataletsel navigasyon sistemleri içerisinde en sık kullanılan ivmeölçer tiplerinden birisidir. Bu tez, KSİ için kapsamlı bir matematiksel modelin geliştirilmesi ve doğrulanması üzerine odaklanmakta ve bu sensör tipinin anlaşılmasını ve dinamik performans değerlendirmesini artırmayı amaçlamaktadır. Çalışma, ivmeölçerin hem açık devre hem de kapalı devre sistem olarak modellenmesini içermekte ve sunulan bu modeller daha sonra açık döngü ve kapalı döngü test prototipleri üzerinde yapılan testler ile deneysel olarak da doğrulanmaktadır. Deney sonuçları, geliştirilen modelin doğruluğunu ve güvenilirliğini onaylamakta, sensörün gerçek uygulama senaryolarında dinamik davranışını öngörebilme yeteneğini göstermektedir. Ayrıca, kapalı devre sistem modeli kullanılarak çeşitli tasarım parametrelerinin dinamik performans üzerindeki etkileri de incelenmektedir. Son olarak, doğrulanmış bu kapalı devre sistemin KSİ'lerin ileriki optimizasyon ve tasarım iyileştirme çalışmalarına yüksek-sadakatli bir model olarak hizmet etmesi de beklenmektedir.

Anahtar Kelimeler: Kuvars Sarkaçlı İvmeölçer, Ataletsel Sensör, Kapalı Devre Sistem Modelleme, Deneysel Doğrulama, Yüksek Sadakatli Model

To My Family

ACKNOWLEDGMENTS

Firstly, I would like to express my infinite gratitude to my thesis supervisor, Assoc. Prof. Dr. Melin Şahin and co-supervisor Assist. Prof. Dr. Gökhan O. Özgen, for providing me the opportunity to work with them, dedicating their invaluable time, always approaching with patience, tirelessly sharing their knowledge and ideas and for all the technical insights they have generously offered throughout the research.

I would like to thank my company Roketsan Missiles Incorporation for all contributions to my engineering career, giving me a chance to study on such a valuable topic and letting me use experimental equipment.

I would like to express my gratitude to my managers Dr. Caner Gençoğlu, Mustafa İnci and Dr. Alper Ünver, for their consistently positive approach, sharing of technical knowledge, guidance in showing me the right path and their provision of all sorts of convenience throughout the research. I will always be grateful to them.

I would like to thank my colleagues and friends Hasan Yetgin, Tevfik Ozan Fenercioğlu, Özkan Kahveci, Denizhan Yerel, Recep Berk Avcıoğlu, Eray Humalı, Yunus Emre Öztaş, Zekai Uygur Zeren, Eren Koçak, Yasin Cihaner, Kadir Erdem, Ümit Bektik and Özgür Kolcu for their endless support and motivation.

I would also like to thank my dear friends Doğancan Bahan, Hasan Akman and Ersin Altın for their supports.

I am grateful to my parents and sister Nesrin, Şevket and Bengü for their support, confidence and endless love.

Finally, I would like to express my gratitude to love of my life Kübra for always believing in me, supporting my endeavors, making my life easier and always caring for me more than I do for myself.

TABLE OF CONTENTS

LIST OF TABLES

TABLES

LIST OF FIGURES

FIGURES

LIST OF ABBREVIATIONS

ABBREVIATIONS

CAD	: Computer Aided Design
CVG	: Coriolis Vibratory Gyroscope
FEA	: Finite Element Analysis
FEM	: Finite Element Method
FOG	: Fiber Optic Gyroscope
GNSS	: Global Navigation Satellite System
IMU	: Inertial Measurement Unit
INS	: Inertial Navigation System
RLG	: Ring Laser Gyroscope
SFD	: Squeeze Film Damping
QFA	: Quartz Flexible Accelerometer
VRE	: Vibration Rectification Error

CHAPTER 1

INTRODUCTION

1.1 Background and Motivation of the Study

Navigation systems play a crucial role in guiding and tracking moving objects across various domains. Their importance stems from their ability to determine and manage the position, direction and movement of objects accurately. Various sensors are used to gather data about the object's movement, orientation and surrounding environment in a navigation system. The most preferred sensors can be listed as the Global Navigation Satellite System (GNSS) receivers, inertial measurement units (IMUs), magnetometers, barometers and altimeters [1–5].

Inertial navigation is a navigation technique that relies on the use of an IMU which contains inertial sensors such as accelerometers and gyroscopes, installed within a moving object to determine its position, orientation and velocity relative to an initial starting point. This type of system functions based on the principle of Newton's laws of motion. It works by measuring the acceleration and angular velocity of the object in which they are installed. Accelerometers detect changes in velocity, while gyroscopes measure changes in orientation. By continuously integrating these measurements over time, an inertial navigation system (INS) can calculate the object's current position, velocity and orientation. As an advantage, this navigation method is self-contained and operates independently of external references, such as GNSS signals. It finds applications in various fields, including military vehicles, aerospace, marine navigation, autonomous vehicles, robotics and more, where continuous and real-time positioning and orientation information are essential, especially in environments where external signals might be unreliable or unavailable. However, INS accuracy may degrade over time due to inherent sensor errors, known as drift, which accumulates over prolonged periods. To mitigate this, INS is often

integrated with other navigation systems like GNSS for periodic updates to correct errors and improve accuracy. On the other hand, the dynamic characteristics of inertial sensors play a critical role in the accuracy of the system. Some can be listed as dynamic measurement range, response to shock loads and stability under vibration loads. To achieve the desired dynamic performance, it is necessary to accurately model the sensor structure and make appropriate design changes when needed.

Quartz Flexible Accelerometer (QFA) is a single-axis, non-gyroscopic type inertial sensor that measures translational acceleration. It is called a force rebalance accelerometer since it works in a closed loop manner to hold sensitive element inside by rebalance force. Due to long term stability and accuracy characteristics, QFAs are one of the most used accelerometers in strapdown inertial measurement units. This study aims to achieve an experimentally verified system model and observe dynamic characteristics of the QFAs for different system parameters.

1.2 Objectives of the Study

The main objective of this thesis is adding a novel contribution to the literature by providing a complete modelling methodology for QFAs, including the model of squeeze film damping (SFD) in the system. All objectives can be given in detail as below:

- Define all components of the system in detail,
- Model each component of the system,
- Model SFD in the system by finite element analysis (FEA),
- Model accelerometer as an open loop system,
- Verify open loop accelerometer system model by experiments,
- Model accelerometer as a closed loop system,
- Verify closed loop accelerometer system model by experiments,
- Investigate effects of different parameters in the system on dynamic performance which is comprised of frequency and shock responses.

1.3 Limitations of the Study

The major limitations of the study are listed as follows:

- The pendulum in the system is modelled as a single degree of freedom rotational system and therefore higher order vibrational modes are neglected.
- The effects of tolerances of mechanical and electronical parts and assembling of them are neglected.
- Temperature dependence of any system parameter is neglected. All experimental work is conducted within the range of 20 to 26 ℃ room temperature.
- All inertial sensors have a different output behavior for a short time just after they are powered, called as warm-up period. Therefore, the initial 30-minute waiting period is set prior to each test.
- Frequency responses of the closed loop system are investigated in 100-2000Hz frequency range. Mechanical shaker ability limits the lowest frequency value and interested frequency range limits the highest frequency value.
- Although obtained closed loop model is verified by sine sweep and mechanical shock tests, it is not verified for random vibrational loads in this particular study.
- PZT based accelerometer with high bandwidth is used as reference during experimental verification of closed loop system model. It is assumed that frequency responses of these accelerometers are flat between 20-2000Hz frequency range.

1.4 Outline of the Thesis

This thesis comprises six main chapters. In Chapter 1, motivation of the research study, its main objectives, limitations and assumptions made are introduced. In

Chapter 2, a comprehensive literature review about inertial navigation, inertial sensors, pendulous type accelerometers and SFD in accelerometers is given.

In Chapter 3, first, all the parts and components in QFA are described in detail. Working principle of the accelerometer is defined by simple schematics of the system. Then, each component in the accelerometer system is modelled by analytical or numerical calculations to be used in system-level models. Pendulum in the system is modelled as a single degree of rotational system. Moment of inertia of the pendulum is obtained by CAD software and rotational stiffness is obtained by analytical derivations. Rotational damping is assumed to include only SFD which is modelled by finite element modelling (FEM) and analyzed through finite element analysis (FEA) and depend on the displacement of the pendulum. Magnetic force due to coil excitation is modelled as Lorentz force and magnetic flux density on the coils are characterized experimentally. On the other hand, controller in the sensor electronics is modelled as a PID controller. Finally, electronic modelling of torquer coils and readout circuit is given in s domain.

In Chapter 4, QFA is modelled both as an open loop system and closed loop system. Open loop system model includes sensor electronics without controller. Test prototype working in an open loop manner is described and then is used in characterization and verification experiments. First, capacitive pickoff gain is characterized by open loop tests. Then, the open loop system model is experimentally verified by comparing step responses of the open loop test prototype in time domain. Next, QFA is modelled as a closed loop system, which includes controller in sensor electronics. The closed loop system model is experimentally verified by sine sweep and mechanical shock tests. Finally, both frequency and shock responses of the simulations and tests are compared.

In Chapter 5, the closed loop model obtained in Chapter 4 is used to investigate the effects of some design parameters on dynamic performance of the system. First, different readout circuits are defined and in order to obtain better dynamic behavior, new readout circuits are introduced including load capacitors. Simulation results for

all configurations are given as frequency responses of the output, pendulum displacement and shock response of the system. Also, effects of SFD in the system are investigated by simulations which include increased SFD.

In Chapter 6, a general conclusion about thesis study and the outputs of it are given. Finally, recommended future study topics are provided in detail.

CHAPTER 2

LITERATURE REVIEW

2.1 Introduction

Any platform travelling from a specific location to another needs a navigation system to move in a desired way. They are also used to obtain instantaneous attitude information. IMUs can provide acceleration, velocity and position traveled from the initial state without being dependent on external measurements. Therefore, these units are indispensable for many applications where connection to the outer references are limited. IMUs include inertial sensors capable of measuring acceleration along translational and rotational directions. Pendulum type accelerometers are among the most used sensors within these units to determine acceleration along the translational direction. In this section, a comprehensive review of literature about inertial navigation, inertial sensors, pendulous type accelerometers and SFD in accelerometers is given.

2.2 Inertial Navigation and Inertial Sensors

An INS is mainly comprised of a set of inertial sensors and a navigation computer in general. Inertial sensors provide instantaneous acceleration information along all degree of freedoms. Navigation computer calculates the current position based on the previously known position, direction and speed of travel which is known as dead reckoning [1]. In result, dead reckoning along all three orthogonal axis using inertial sensors and navigation algorithm forms the INS. The process relies on continuously updating the position by accounting for the distance traveled in a particular direction from a known starting point. It considers factors such as accelerations, time and direction changes to project the current position. An INS does not require any

external reference which is the biggest advantage of that type of navigation system. However, change in position is calculated by double integration of acceleration during operation that may cause dramatic errors in long term navigation results depending on the performance of inertial sensors [1–4]. Especially noise and long-term stability of the bias and scale factor performances of inertial sensors directly affect that performance. To compensate this, most of the modern inertial navigation systems are aided by GNSS [2] providing position information. Principles of it are based on the functioning of satellite constellations that transmit signals to receivers on Earth. In short term usage, position errors of GNSS are higher than position errors of INS. On the other hand, position accuracy performance of INS degrades over time but remains constant for GNSS. Therefore, complete systems are preferred as GNSS aided INS in most of the applications to benefit from advantages of both technologies together. Main components of a GNSS aided INS is given in Figure 2.1.

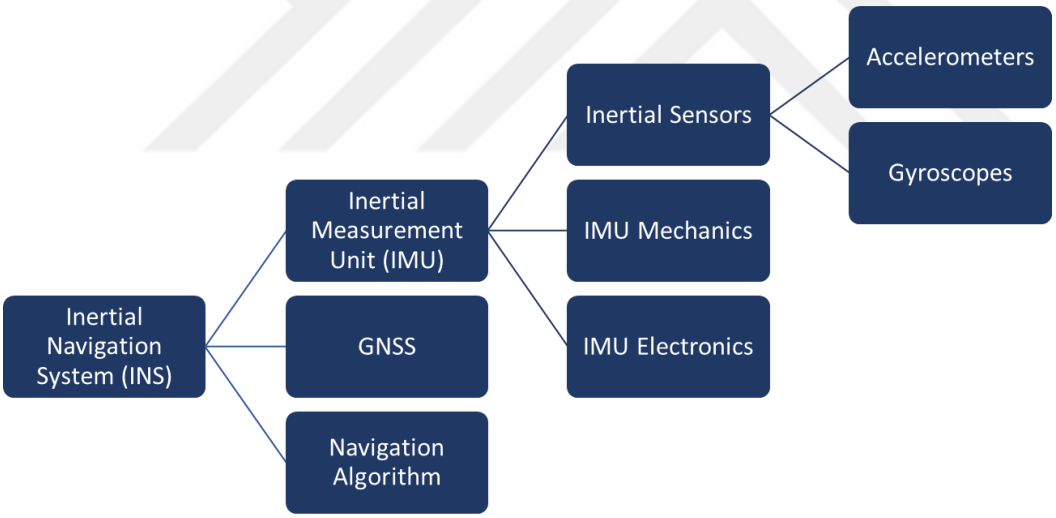

Figure 2.1. Components of a GNSS Aided INS

A mechanical IMU structure comprised of inertial platforms, accelerometers, gyroscopes and gimbals to maintain position of the platforms are used in earlier times [2, 3]. This mechanical IMU structure uses gimbals to maintain positions of the platforms and thereby accelerometers. Gyroscopes are mounted on the platform, not for measuring the rotational acceleration but for measuring the unwanted platform

rotations and send signal to the gimbal structure to compensate them. Main advantages of this type of structure are listed below [1–5]:

- The attitudes of accelerometers are held constant. Only one accelerometer in the system is exposed to gravitational acceleration. Therefore, accuracy of two other accelerometers increase.
- Gyroscopes are not used for measuring the rotation of the moving vehicle. They are only used to measure small, undesired rotations to send signal to the gimbal structure for compensation of rotation. Therefore, simple gyroscopes can be used. Also, small rotations decrease rate-dependent errors of accelerometers.
- Each platform may rotate full cycle. This ability allows re-calibration of the accelerometers and increases long term navigation performance.

However, due to the complexity of the mechanical structure, these types of structures have disadvantages in terms of reliability, cost, weight and the space they occupy. As a result of technological improvements in electronics, optics and inertial sensors strapdown systems are introduced with simpler mechanical structures. Strapdown systems are directly mounted to the moving vehicle and share the same axis system. To be able to measure translational and rotational accelerations along all six degrees of freedom, at least three accelerometers and three gyroscopes are used in a strapdown IMU. A simple schematic illustration that shows both gimbaled and strapdown structures is given in Figure 2.2.

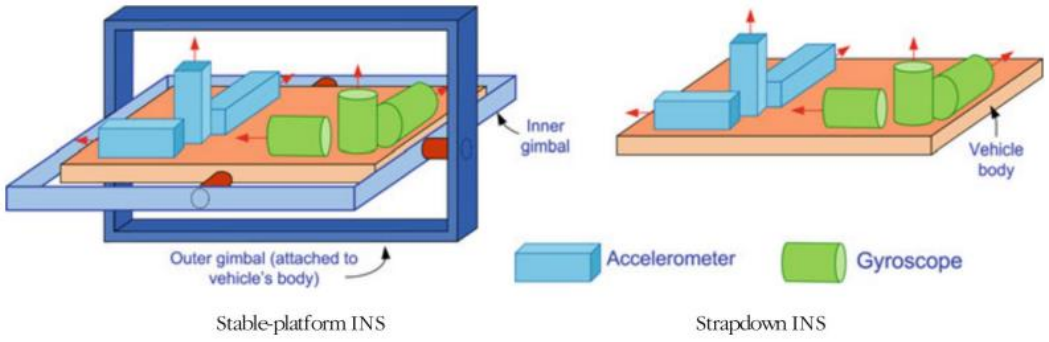

(a) (b)

Figure 2.2. Schematic Illustrations of (a) Gimballed and (b) Strapdown INS [6]

In general, inertial sensors of a strapdown IMU are mounted on a mechanical structure orthogonally. IMU electronics supply power to the inertial sensors, obtain acceleration outputs of them, calculate velocities and provide acceleration and velocity information to the outside of the IMU.

Although MEMS type inertial sensors have cost and size advantages, their performances are not enough to be used in high end navigation applications [7]. In high end navigation, there are mainly two types of gyroscopes. The first one, optical gyroscopes function based on the Sagnac effect, where light travels in opposite directions in an optical path. A phase shift due to the rotation of the optical path is experienced which is correlated with angular rate (Figure 2.3).

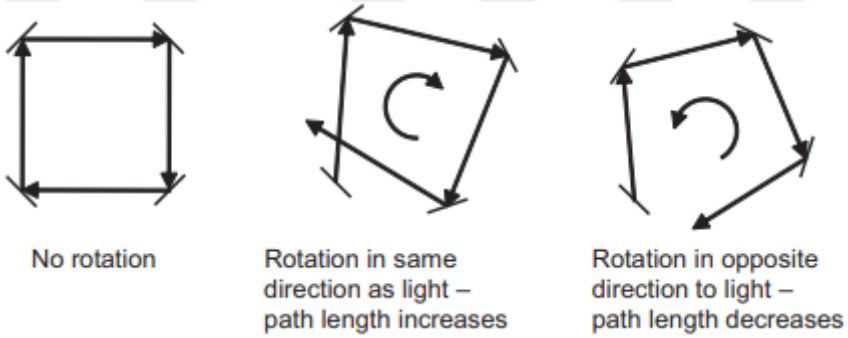

Figure 2.3. Sagnac Effect on Rotating Optical Path [1]

There are two types of optical gyroscopes function based on the Sagnac effect, Ring Laser Gyroscope (RLG) and Fiber Optic Gyroscope (FOG). RLG is a highly sensitive inertial sensor that detects angular rates by exploiting the interference of laser beams traveling in opposite directions within a closed-loop optical cavity (Figure 2.4). As the gyroscope or the cavity undergoes rotation, the Sagnac effect induces a phase difference between the counter-propagating laser beams, allowing for the precise measurement of angular motion [8]. FOG is a competitive technology against RLG that measures angular rates utilizing the principles of light interference within coiled optical fibers (Figure 2.5). Operating based on the Sagnac effect, FOGs split light into two beams traveling in opposite directions within a closed optical fiber loop. When the gyroscope or the fiber experiences rotation, a phase shift occurs between the light waves, enabling the detection of angular rate [9].

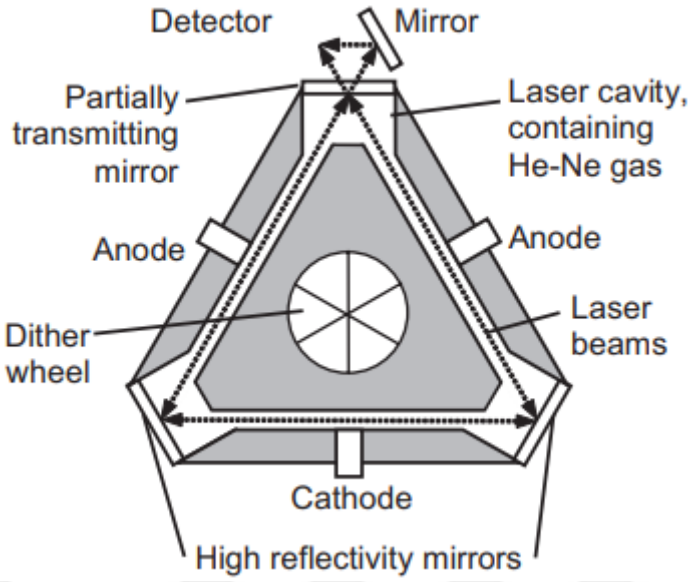

Figure 2.4. Schematic Representation of Typical RLG [1]

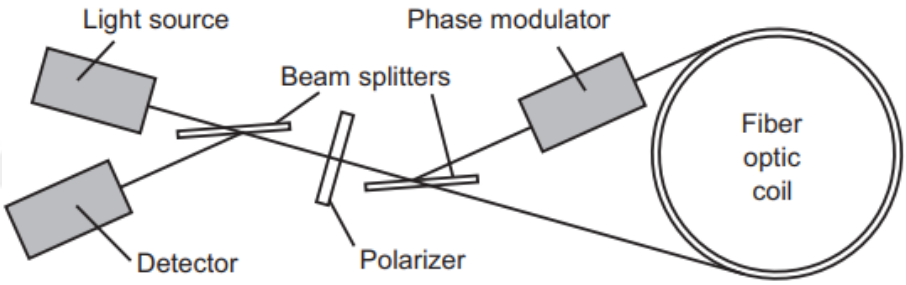

Figure 2.5. Schematic Representation of Typical FOG [1]

The second type of gyroscopes is vibratory gyroscopes. Coriolis Vibratory Gyroscope (CVG), is a vibratory type of gyroscope utilizing the Coriolis effect to measure angular velocity or changes in orientation. This gyroscope operates by inducing vibrations in a resonating structure and detecting the Coriolis force induced by angular motion, causing a phase shift in the vibrating structure. CVGs are known for their compactness, low power consumption and high precision [10, 11].

2.3 Pendulous Type Accelerometers as Inertial Sensors

Acceleration on a body, which is named as proof mass in the Figure 2.6 presenting a conceptual design of an inertial accelerometer, causes inertial force on it which equals to mass times acceleration. Due to Newton's first law of motion, proof mass displace relative to the housing. By sensing displacement, one can obtain a primitive single degree of freedom inertial accelerometer since the system gives a response linearly dependent on exposed acceleration.

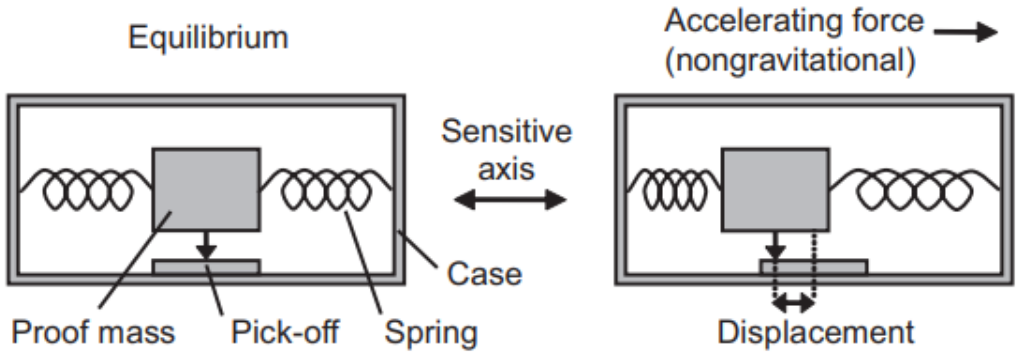

Figure 2.6. Conceptual Design of an Inertial Accelerometer [1]

One of the major challenges in designing inertial accelerometers is to design a structure that allows proof mass to move freely along the sensitive axis while keeping it rigid in other axes to prevent movement. Pendulous accelerometers operate based on the principle of a proof mass suspended on a pendulum or flexible support within a housing. When subjected to linear acceleration, the inertial force acting on the proof mass causes it to displace relative to its housing due to Newton's first law of motion. This displacement induces a torque that tilts the pendulum or flexes the support structure, generating a measurable angular displacement. The angular displacement is typically detected using capacitive, piezoelectric, or optical sensing mechanisms. Capacitive sensors measure changes in capacitance due to alterations in the gap between the proof mass and fixed electrodes, while piezoelectric sensors detect stress-induced changes in material properties and optical sensors gauge variations in light intensity caused by the angular movement. This displacement is

converted into an electrical signal proportional to the applied acceleration, providing an output indicative of the acceleration magnitude. Pendulous accelerometers are advantageous for their ability to measure both static and dynamic acceleration and are commonly employed in INS. Schematic representation of a pendulous type accelerometer is given in Figure 2.7.

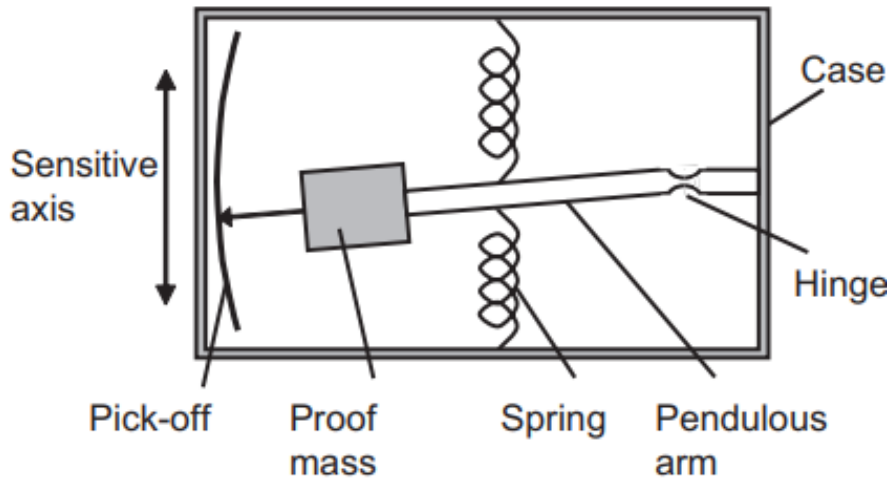

Figure 2.7. Schematic Representation of a Pendulous Type Accelerometer [1]

Accelerometer given schematically in Figure 2.7 is an open loop type inertial accelerometer and when proof mass displacement increases, acceleration level increases. Although it is practical to design and produce an open loop accelerometer, there are three main disadvantages of working in an open loop manner:

- As acceleration increases, displacement also increases. High acceleration values may exceed the displacement limits of the pendulum or the pickoff measurement limits, which leads to low measurement range. Spring or pendulum may be redesigned to decrease displacement per acceleration amplitude, which also reduces resolution of the sensor output. In result, measurement range and resolution have an inverse relationship.
- Springs in the system have mechanical hysteresis and some degree of nonlinearity. These characteristics reduce repeatability or, in other words, long term stability and linearity of the sensor.

- Sensitive axis of the sensor rotates as acceleration and thereby displacement level increases.

To resolve this problem, force rebalance type inertial accelerometers work in a closed loop manner. Closed loop accelerometers operate based on a control mechanism that continuously adjusts to maintain a reference position for the proof mass within the sensor. These sensors feature a feedback loop where the output signal of pickoff is used to make real-time corrections, ensuring the proof mass remains at a fixed or null position despite external acceleration level. Any displacement from this set point generates an error signal, prompting the control system to apply corrective forces, typically achieved using electrostatic, piezoelectric, or electromagnetic mechanisms. The feedback loop continuously monitors and adjusts the applied force to counterbalance external acceleration. Hinges are designed such that mechanical hysteresis are minimized but stresses under dynamic loads are lower than yield stress [12]. A schematic representation of force rebalance type accelerometers is given in Figure 2.8.

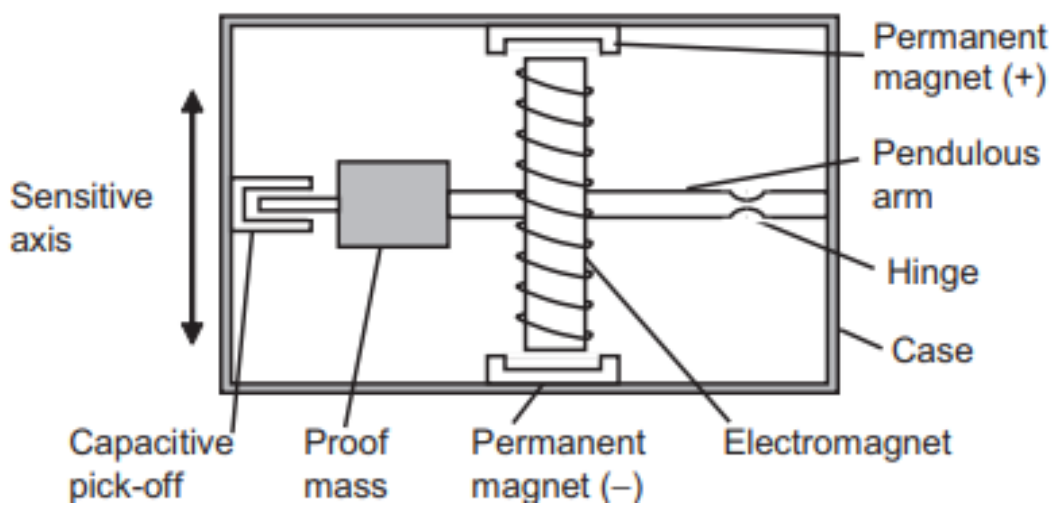

Figure 2.8. Schematic Representation of a Pendulous Type Accelerometer [1]

There is a specialized accelerometer design called Quartz Flexible Accelerometer (QFA), or in general 'Q-Flex,' and it stands out as one of the most successful examples in terms of mass, price and performance within its category of pendulous

type accelerometers. Developed through years of research and accumulated knowledge, this design originated in the 1970s [13] and continues to maintain its popularity in the field of navigation systems with minor modifications in present times. A schematic illustration of QFA is given in Figure 2.9.

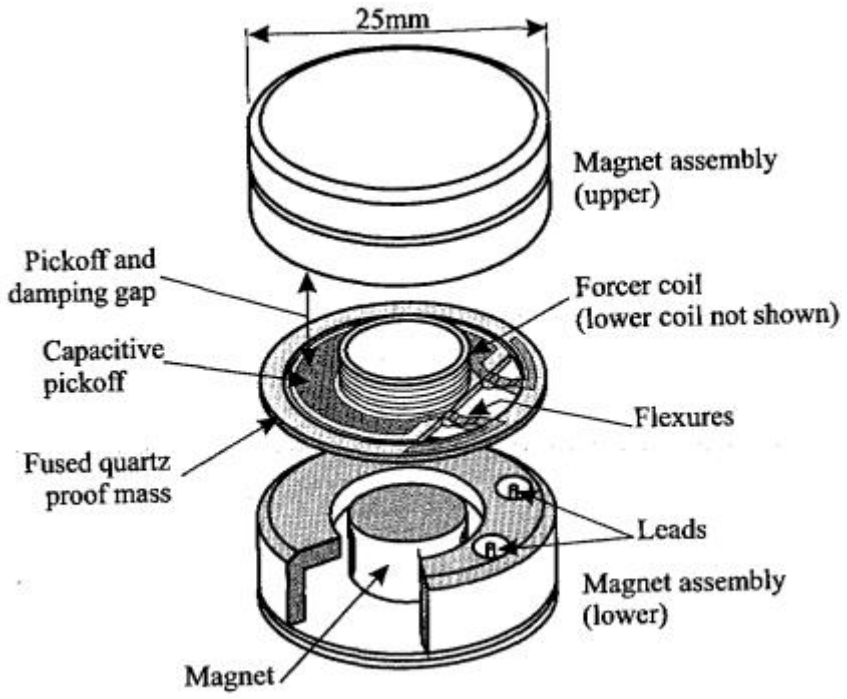

Figure 2.9. Schematic Illustration of the QFA [3]

QFA structure has double hinge type structure to connect pendulum to the rigid part, use capacitive pickoff to sense motion of the pendulum and use magnetic structures to provide magnetic feedback force on pendulum against inertial force. Material of pendulum, quartz and material of magnetic cases, special nickel-iron alloys have low coefficient of thermal expansion properties [3]. Also, quartz material has low mechanical hysteresis [3]. Additionally, dual hinge structure facilitates the desired bending deflection but hinders undesired torsional deflections of the pendulum. In result, this closed-loop, single-axis accelerometer stands out for its low temperature dependency, high long-term stability and low noise characteristics.

2.4 Squeeze Film Damping in Accelerometers

In some of the MEMS and larger sized pendulous type of accelerometers, displacement of the pendulum is sensed by using capacitive pickoff. This type of structure consists of a stationary surface and the surface of the pendulum moving against it. Displacement of the pendulum results in capacitive change and in this way, the movement is detected. Capacitive surfaces may also be used to provide capacitive forcing in some types of devices. To increase sensitivity of the capacitive pickoff or the capacitive forcing, air gap between the so called moving and stationary surfaces are designed to be as small as possible. In a dynamic working condition, some portion of air in the gap flows out or air from outside flows into the gap. This type of gas motion causes a rise or a drop on air pressure in the gap. In both cases, a special type of force is formed on moving surface in the opposite direction to the motion. These squeeze film effects become dominant in such systems if the width of the moving plate to the air gap ratio is higher than three [14].

Squeeze film phenomena in the gas in between moving and stationary surfaces mostly take place due to inertial and viscous effects. Inertial effects are mostly neglected in the MEMS and pendulous type accelerometers since their small size geometry. In result, Reynolds equation and its linearized form are mostly used to model fluid flow in these types of devices. A comprehensive and general overview on the SFD effect, important parameters and calculation methods in MEMS devices are presented in [14, 15].

There are more than one design criteria to achieve desirable squeeze film effects in accelerometers. Input-output frequency response and shock response are two critical dynamic behaviors of such systems. If mechanical structure is designed correctly, SFD in the system may help to achieve necessary frequency response. Moreover, it assures protection against high amplitude mechanical shocks. On the other hand, most of the MEMS devices operate based on the principle of vibration at the resonant frequency of the moving structure. In such oscillatory systems high quality factor is desired, which is inversely related to damping in the system. Therefore, it is essential

to reduce the effects of SFD as much as possible. In some of the accelerometers transversely moving perforated plates are preferred to reduce SFD effects. Estimation of squeeze effects in such systems are crucial in designing of them. Various studies focus on modelling and validation of models for SFD effects in structures with perforated plates [16–20].

In some micro-nano scale resonator structures working in a low ambient pressure environment, continuum models cannot be used to model squeeze film effects. In such systems gas rarefaction effects are not negligible and have to be considered in SFD modelling [14, 21–25]. To model rarefaction effects, effective dynamic viscosity is used in Reynolds equation instead of dynamic viscosity of the gas.

Squeeze number is introduced in [26] which gives information about gas compressibility. It includes the geometrical parameters, gas properties and frequency of the motion as well. Gas behaves as a damper in systems with low squeeze numbers whereas at high values of squeeze number it cannot escape between two surfaces, squeezes and starts to act like a spring [27]. The gas effect should be modeled both as a spring and a damping element together according to the squeeze number.

Although the moving part operates with low displacements in most of the systems, some systems work with high displacements. In such cases, the amplitude ratio parameter which expresses the ratio of the displacement to the air gap becomes significant. Modelling of such amplitude effects at low squeeze numbers are analytically modelled in [28, 29].

Relative pressure on border of the moving plate is mostly assumed as zero in calculations on squeeze effects. This is a valid assumption if lateral dimensions of the moving plate are much bigger than the air gap. Otherwise, border effects take place and they need to be considered in modelling squeeze film effects. There are some studies focused on calculating effective lateral dimensions of the plate to use them in analytical models instead of original dimensions [30–34]. A complete model comprising both border and amplitude effects are proposed in [22][35].

Great effort is devoted to modelling and characterization studies on squeeze film effects in various devices such as accelerometers, optical switches and micro actuators. Moeenfard [36] investigates SFD effects in torsional micro actuators. Flexible microstructures under SFD effects are analyzed by Nayfeh and Younis [37]. Nontrivial geometries are modelled by using FEM. In [38] both damping and noise terms due to squeeze film effects are investigated. Chen and Kuo [39] propose a numerical procedure to model squeeze and viscous damping in micro electrostatic comb drives. Sun et al. investigate effects of squeeze film damping on switching time of a micro scaled optical switch [40]. Mo et al. [41] proposed an open loop test method to characterize damping due to squeeze film effects in MEMS accelerometers. In [42] squeeze film effects in nonlinear capacitive circular microplates are modelled and characterized experimentally. However, there are no specific studies in the literature focusing on modelling of SFD and its effects in QFA type inertial sensors.

2.5 Conclusions

In this section, a brief summary about inertial navigation and inertial sensors, pendulous type accelerometers, QFAs and SFD in accelerometers are given. Inertial sensors and thus QFA type accelerometers are used in navigation systems of moving vehicles. Therefore, obtaining mathematical models of such sensors used under dynamic load conditions and identifying their dynamic behaviors through simulations hold significant importance for design and optimization studies. Furthermore, the presence of SFD in the system level model is crucial, which is effective within QFA due to its geometric characteristics.

CHAPTER 3

MODELLING OF COMPONENTS IN THE QUARTZ FLEXIBLE TYPE ACCELEROMETER

3.1 Introduction

Quartz pendulum accelerometers contain various subsystems based on multiple physical principles to measure the acceleration. To obtain the dynamic characteristics of the system, it is necessary to model each component separately and integrate them into a closed-loop system model. For this purpose, in this section, all mechanical and electronical components of the system are introduced, their working principles are explained and each component is modeled individually by analytical calculations, experiments and FEM.

3.2 Description of a Quartz Flexible Type Accelerometer

QFA is a single axis non-gyroscopic inertial sensor that senses translational acceleration [43]. In general, this type of accelerometers reach resolution lower than $1\ \mu g$ and bandwidth beyond $1\ kHz$. Long term stability of the sensor parameters depends on design and manufacturing processes but control, tactical and navigational grade sensors are available in the market as QFAs.

With its compact design, the QFA takes up minimal space and facilitates easy assembly. When observed from the outside, there is an outer case produced by stainless steel containing a two, three or four-legged mechanical mounting interface and an outer cover containing electronic interfaces to the external world. The mechanical mounting interface may vary based on the sensor design. Each pin on the outer cover is utilized for supplying power to the sensor, transferring acceleration

output to the outside, transmitting temperature sensor signal to the outside if present internally and facilitating connections for various test signals, if needed.

There is a mechanical sensing core assembly and sensor electronics inside the outer case and cover. Simple schematic of the accelerometer system including a mechanical sensing core assembly and sensor electronics is given in Figure 3.1.

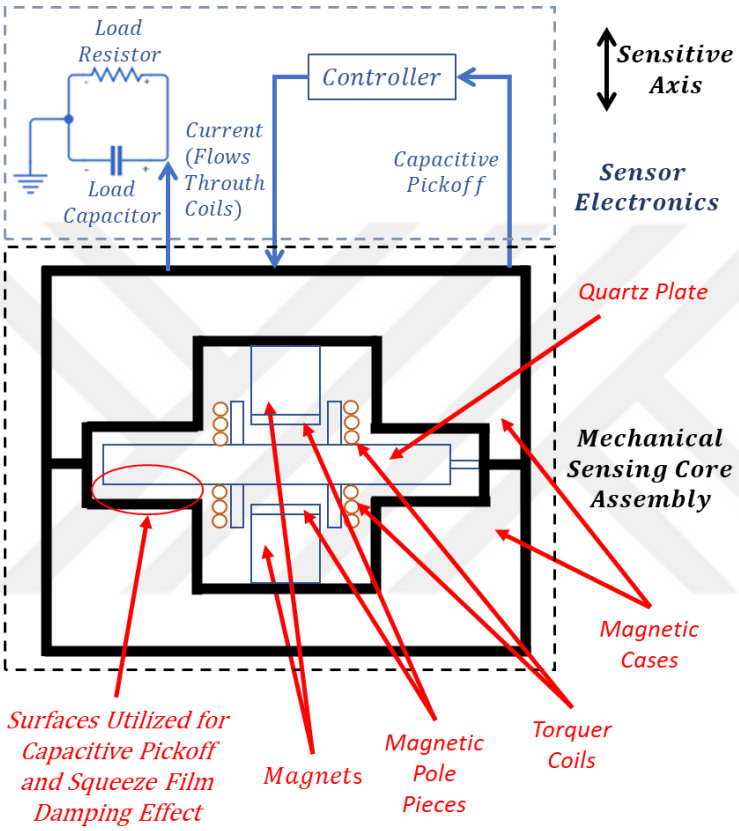

Figure 3.1. Schematic of the Accelerometer System

As seen in Figure 3.1, mechanical sensing core assembly is comprised of quartz plate, torquer coils, magnetic cases, magnets and magnetic pole pieces. Quartz plate and one coil on each side of it are rigidly connected to each other and forms the quartz plate-coils assembly which is given in Figure 3.2(a). Magnetic case, a magnet and a magnetic pole piece are rigidly connected to each other and they form the magnetic case assembly which is given in Figure 3.2(c). In a mechanical sensing core assembly, there is one quartz plate-coils assembly placed in between two

magnetic case assemblies. Sensor electronics is connected to the mechanical sensing core assembly. It includes electronic components of the capacitive pickoff demodulator and a controller.

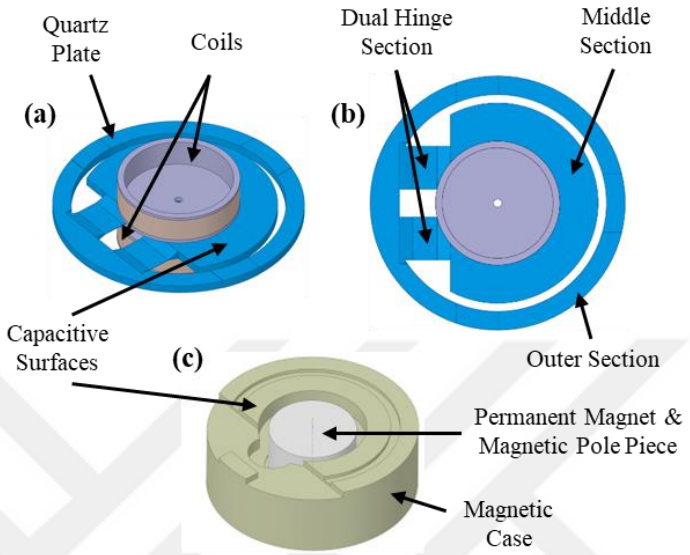

Figure 3.2. (a) Isometric view of quartz plate-coils assembly: (b) Top view of quartz plate-coils assembly and sections of quartz plate, (c) Isometric view of magnetic case assembly

As seen in Figure 3.2(a) and Figure 3.2(b), there is a wet-etched quartz plate and two coils on it in the quartz plate-coils assembly. Quartz plate is a monolithic part composed of the middle section, the outer section and the dual hinge section. Middle section of it has one coil on each side and forms the pendulum of the system. It is connected to the outer section by dual hinge section. Quartz plate-coils assembly is connected to the magnetic case assemblies by touching from outer ring of the quartz plate. Thickness of middle and outer sections of quartz plate is identical and generally in between 600-800µm whereas thickness of dual hinge section is generally in between 15-25µm. Therefore, hinges are assumed to be flexible and other sections of quartz plate are assumed to be rigid. Due to flexibility of hinges, acceleration induces inertial force on the pendulum and deflects it.

Some specially designed sections of the quartz plate are coated with conductive material. These coated surfaces and opposing surfaces of the magnetic metal cases are named as capacitive surfaces (Figure 3.2(a) and Figure 3.2(c)) and they form two capacitor elements on top and bottom of the quartz plate. These capacitors and demodulator in the sensor electronics forms the capacitive sensing arrangement which is used to capture displacement of the pendulum. When there is no acceleration, capacitance values of these capacitors are equal. However, deflection of the pendulum causes capacitive difference which is used to sense displacement of the pendulum. Corresponding signal from demodulation component of the sensor electronics is fed to the controller.

As seen in Figure 3.2(c), magnetic case assembly is composed of a nickel-iron alloy case which is a soft magnetic material, a permanent magnet and a magnetic pole piece produced by a soft magnetic material. In the assembly, permanent magnet is the magnetic flux source, magnetic case is a road for flux and magnetic pole piece is used to adjust direction of magnetic flux vectors as desired. Magnetic case is used to achieve the desired magnetic flux density on torquer coils of the quartz plate-coils assembly. When there is a capacitive difference, a current signal is supplied to the coils from the output of the controller. Due to existing magnetic flux density, the current passing through the torquer coils results in a Lorentz force on the pendulum and holds it on the nominal position. Meanwhile, excitation signal from output of the controller is given to the outside of the accelerometer as a current and read on a load resistor as voltage difference. A capacitor named as load capacitor may be used together with load resistor to filter output of the accelerometer. As a result, accelerometer gives an electrical output correlated with exposed acceleration. Working principle of the accelerometer system in a summarized schematic representation is given in Figure 3.3.

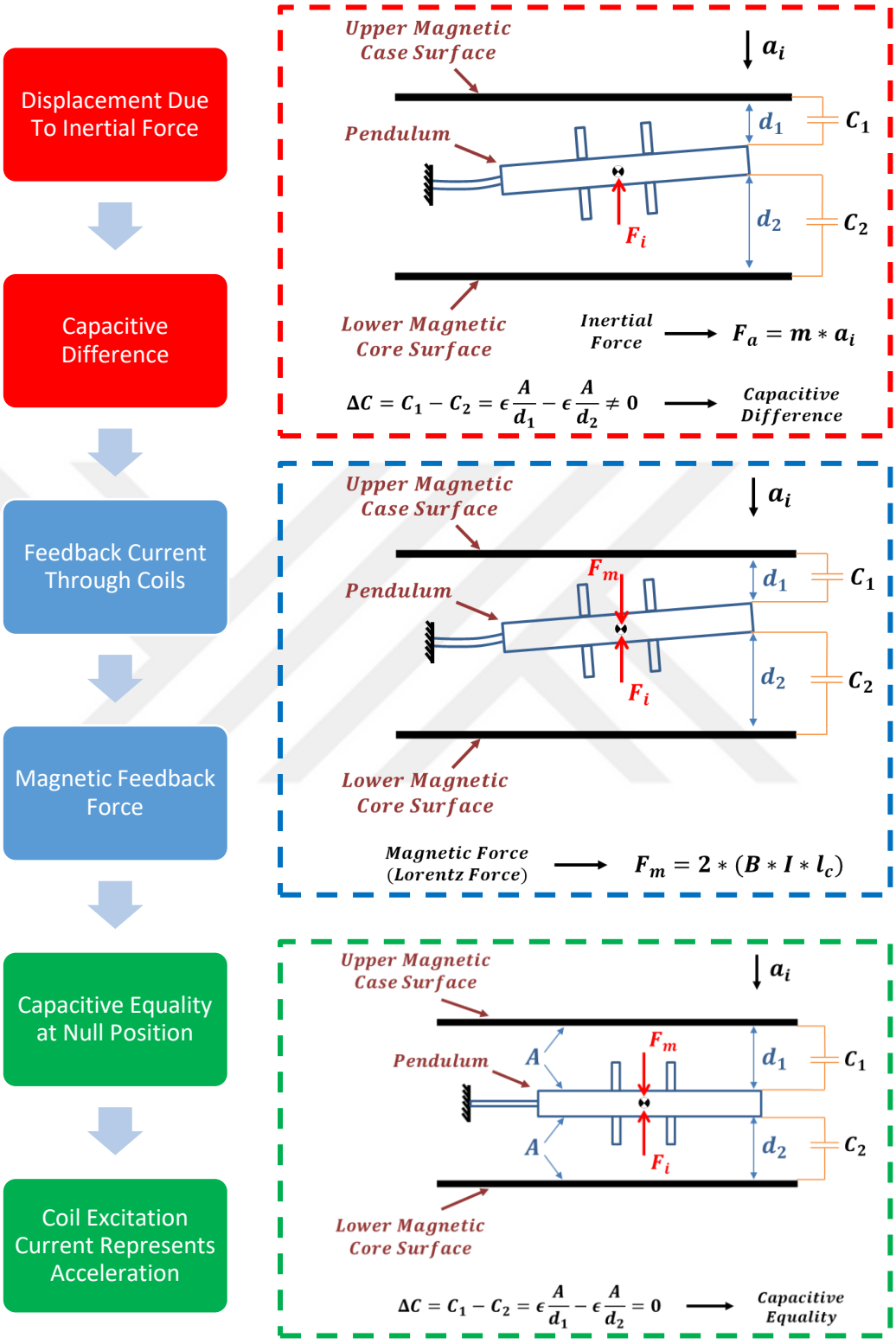

Figure 3.3. Schematic Representation of Working Principle of QFA

In Figure 3.3, upper magnetic case surface and lower magnetic case surfaces are stationary. One end of the pendulum is fixed, which represents the one end of the dual hinge structure connected to the outer section of the quartz plate. F_i and F_m are the inertial force induced by acceleration and magnetic force induced by coil excitation on the pendulum where m, a_i, B, I and l_c are mass of the pendulum, input acceleration, magnetic flux density on coils, excitation current through coils and length of each coil correspondingly. C_1 and C_2 are the capacitance values of each capacitor on each side of the pendulum, where ϵ, A, d_1 and d_2 are dielectric permittivity of the air, surface area of the capacitive surfaces on magnetic cases and pendulum and instantaneous distances from pendulum surfaces to magnetic case surfaces, respectively. For motion of the pendulum, small displacements are assumed to calculate capacitance values for parallel plate capacitors.

On the other hand, resolution of the capacitive pickoff in the system increases as the gap between capacitive surfaces of the pendulum and magnetic cases decreases. Therefore, the system is designed to minimize this gap as much as possible. Lateral dimensions of the pendulum in such systems vary in between 15-25mm and air gap between pendulum and magnetic case surfaces varies in between 15-25µm in general. As a result of the movement of pendulum against the fixed surface of magnetic case, air in between the gap flows out. This causes a pressure change on air in the gap and hence there is a specific type of force on these surfaces (Figure 3.4). Since the surface area of capacitive pickoff surfaces is much bigger than air gap dimension, squeeze film effects become dominant [14].

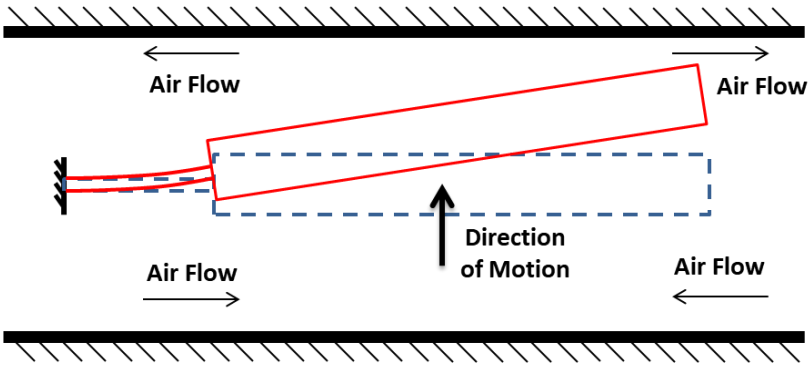

Figure 3.4. Fluid Flow During Movement of Pendulum (*Coils are not shown*)

3.3 Modelling of the Quartz Plate-Coils Assembly

The pendulum of the quartz plate-coils assembly is assumed and modelled as a rotational single degree of freedom system. Forces acting on the pendulum structure is shown in Figure 3.5.

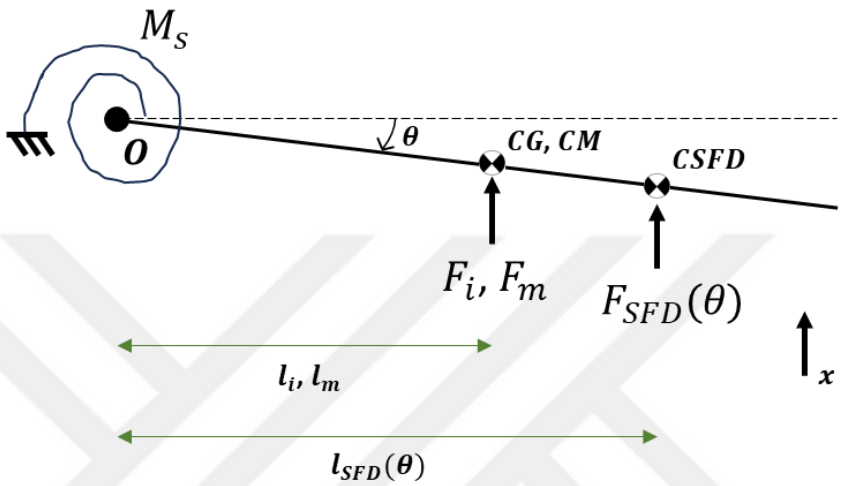

Figure 3.5. Forces Acting on Pendulum Structure (*Coils are not shown*)

where θ indicates the rotation of the pendulum about point O. M_s, $F_{SFD}(\theta)$, F_i, and F_m are the recovery spring torque, force due to the SFD, inertial force and magnetic force. CG, CM, $CSFD$, l_i, l_m and $l_{SFD}(\theta)$ are center of gravity of the pendulum, center of magnetic feedback force, center of pressure due to squeeze film effects, moment arms of F_i, $F_m$and $F_{SFD}(\theta)$, respectively. In an ideal design, CG and CM are identical. Pressure distribution on the pendulum caused by SFD changes with pendulum displacement, thereby $F_{SFD}(\theta)$ and $l_{SFD}(\theta)$ change and torque due to SFD also changes. Because of that, $F_{SFD}(\theta)$ and $l_{SFD}(\theta)$ are modelled depending on rotational displacement θ.

Equation of motion of the pendulum structure is given in Equation (3.1);

$$I_O\ddot{\theta} + C_r(\theta)\dot{\theta} + K_r\theta = F_m(I)l_m + F_i l_i \qquad (3.1)$$

where I_O, $C_r(\theta)$ and K_r are moment of inertia about point O, rotational damping and rotational stiffness coefficients.

In this study, all other sources of damping are neglected except SFD. Therefore, $C_r(\theta)$ only consists of damping due to squeeze film effects. Squeeze film effects cause a distributed load perpendicular to the surface of the pendulum that leads to translational damping coefficient c_{SFD} along x axis. Moment about point O can be expressed as:

$$M_{SFD} = F_{SFD}(\theta)\dot{x}_{SFD}(\theta) = c_{SFD}(\theta)\dot{x}_{SFD}^2(\theta) = c_{SFD}(\theta)l_{SFD}^2(\theta)\dot{\theta} \quad (3.2)$$

where $\dot{x}_{SFD}(\theta)$ is the translational velocity of center of the $F_{SFD}(\theta)$. From Equation (3.2) rotational damping coefficient due to squeeze film effect is identified as;

$$C_r(\theta) = c_{SFD}(\theta)l_{SFD}^2(\theta) \quad (3.3)$$

Modelling of $c_{SFD}(\theta)$ and $l_{SFD}(\theta)$ are given in Section 3.3.2. On the other hand, inertial force simply can be given as:

$$F_i = ma_i \quad (3.4)$$

where m is mass of the pendulum and a_i is the acceleration that accelerometer is exposed along its sensitive axis (shown as x axis in Figure 3.5).

3.3.1 Stiffness and Inertial Modelling of the Quartz Plate-Coils Assembly

Since pendulum in the quartz plate-coils assembly is modelled as a single degree of freedom rotational system, both stiffness and inertia parameters are modelled as a single parameter. Undeformed and deformed pendulum geometry under loading is shown schematically in Figure 3.6.

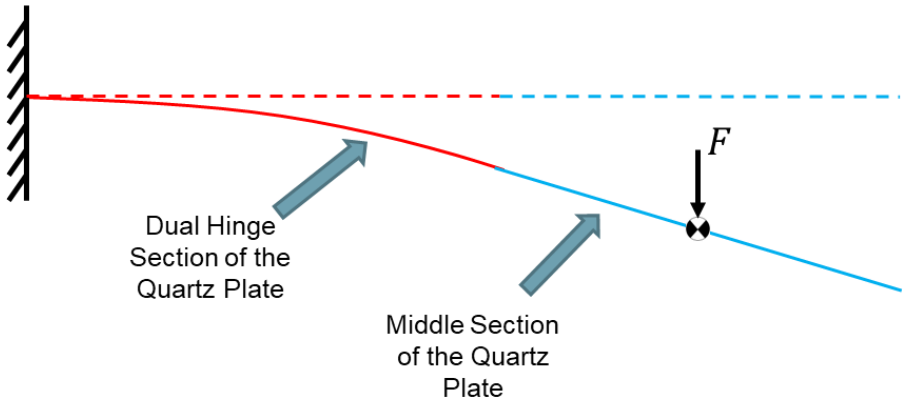

Figure 3.6. Undeformed and Deformed Pendulum Geometry (*Coils are not shown*)

In Figure 3.6, deflected part at left represents the dual hinge section of the quartz plate and rigidly moving part at right represents the middle section of the quartz plate. One end of the dual hinge section is fixed which is the connection point of dual hinge section and outer section of the quartz plate. Undeformed geometry is given with dashed lines and deformed geometry is given with continues lines. As it is given in the same figure, dual hinge section is assumed as flexible and middle section of the quartz plate is assumed as rigid, since thickness of the dual hinge section is approximately 30 times larger than thickness of the middle section. To model rotational stiffness, it is assumed that pendulum is rotating about point O as shown in Figure 3.7.

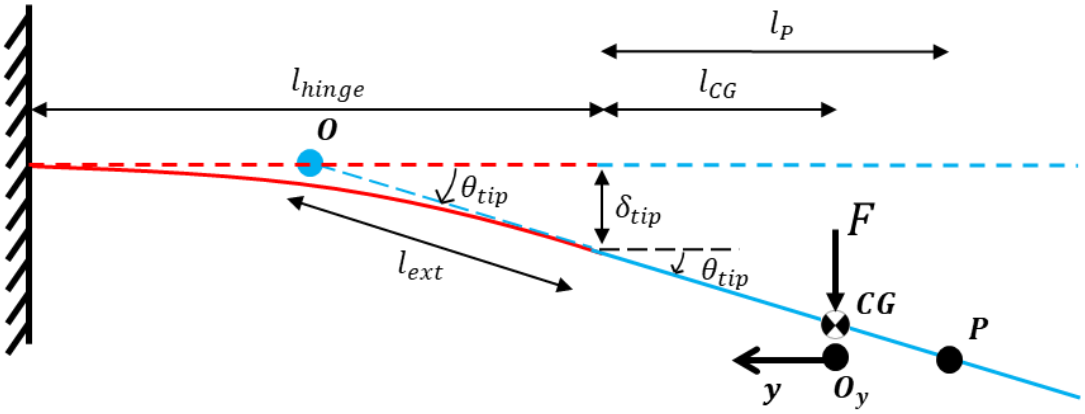

Figure 3.7. Rotation of Pendulum Around Point O (*Coils are not shown*)

In Figure 3.7, CG is the center of gravity of the pendulum where force F is applied on the pendulum. Location of the CG is same with O_y which is the origin of the axis y. l_{CG} defines the distance from CG to the tip of the hinges, l_P defines the distance from any point P on the pendulum to the tip of the hinges and l_{hinge} is the length of the hinges. Parameters δ_{tip} and θ_{tip} are tip deflection of the hinge and angle at the tip when load F is applied on the pendulum. It is assumed that any point P is rotating about point O with rotation radius equal to $l_{CG} + l_{ext}$ where l_{ext} is given in Equation (3.5) for small displacements.

$$l_{ext} = \frac{\delta_{tip}}{\theta_{tip}} \tag{3.5}$$

Rotational stiffness, K_r is defined in Equation (3.6) for the single degree of freedom rotational system.

$$K_r = \frac{F(l_{CG} + l_{ext})}{\theta_{tip}} \tag{3.6}$$

With constant EI_{hinge} assumption along hinge, Equation (3.7) is used to obtain δ_{tip} and θ_{tip}, where E is the young modulus of the quartz plate and I_{hinge} is the area moment of inertia of the hinge which is given in Equation (3.8) [44],

$$EI_A \frac{d^2\delta}{dy^2} = Fy \tag{3.7}$$

$$I_A = \frac{1}{12} w_{hinge} h_{hinge}^3 \tag{3.8}$$

where w_{hinge} and h_{hinge} are total width and height of the dual hinge structure. Equation (3.8) is integrated twice to obtain Equation (3.9) and (3.10).

$$EI_A \frac{d\delta}{dy}(y) = -\frac{Fy^2}{2} + C_1 \tag{3.9}$$

$$EI_A \delta(y) = -\frac{Fy^3}{6} + C_1 y + C_2 \tag{3.10}$$

Constants C_1 and C_2 are obtained and given in Equation (3.13) and (3.14) by using boundary conditions given in Equation (3.11) and (3.12).

$$\frac{d\delta}{dy} = 0 \text{ at } y = l_{hinge} + l_{CG} \tag{3.11}$$

$$\delta = 0 \text{ at } y = l_{hinge} + l_{CG} \tag{3.12}$$

$$C_1 = \frac{F\left(l_{hinge} + l_{CG}\right)^2}{2} \tag{3.13}$$

$$C_2 = -\frac{F\left(l_{hinge} + l_{CG}\right)^3}{3} \tag{3.14}$$

By using Equation (3.10), (3.13) and (3.14), δ_{tip} and θ_{tip} are obtained as below.

$$\delta_{tip} = \frac{F\left(3\left(l_{hinge} + l_{CG}\right)^2 l_{CG} - l_{CG}^3 - 2\left(l_{hinge} + l_{CG}\right)^3\right)}{6EI_A} \tag{3.15}$$

$$\theta_{tip} = \frac{F\left(\left(l_{hinge} + l_{CG}\right)^2 - l_{CG}^2\right)}{2EI_A} \tag{3.16}$$

l_{ext} and K_r are calculated in terms of system parameters by putting Equation (3.15) and (3.16) into Equation (3.5) and (3.6).

$$l_{ext} = \frac{3l_{CG}\left(l_{hinge} + l_{CG}\right)^2 - 2\left(l_{hinge} + l_{CG}\right)^3 - l_{CG}^3}{3\left(\left(l_{hinge} + l_{CG}\right)^2 - l_{CG}^2\right)} \tag{3.17}$$

$$K_r = \frac{2EI_A l_{CG}}{\left(\left(l_{hinge} + l_{CG}\right)^2 - l_{CG}^2\right)} \tag{3.18}$$

On the other hand, moment of inertia about point O, I_O is calculated by Equation (3.19).

$$I_O = I_{CG} + m(l_{CG} + l_{ext})^2 \tag{3.19}$$

where I_{CG} is the moment of inertia about point CG and it is obtained by computer aided design (CAD) software.

3.3.2 Modelling of Damping in Quartz Plate-Coils Assembly

Capacitive surfaces on pendulum and magnetic case are given in Figure 3.8. Squeeze film effects also take place on these surfaces as pendulum moves with a certain velocity. Since displacement of the pendulum is very small, the intersection of the pendulum and magnetic case capacitive surfaces is considered as the effective area for SFD, which is given in Figure 3.9.

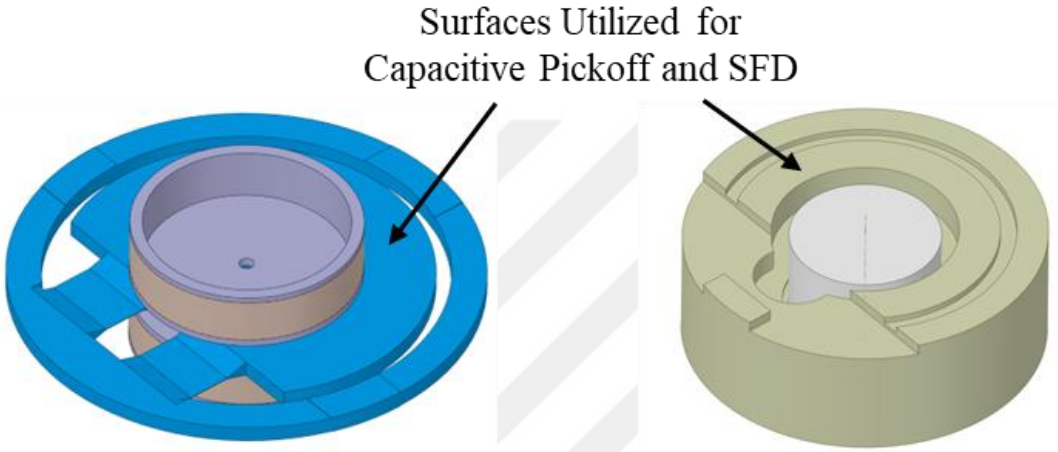

Figure 3.8. Surfaces Utilized for Capacitive Pickoff and SFD

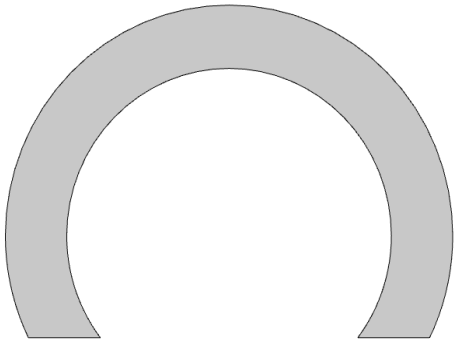

Figure 3.9. Partial Annular Plate Geometry Utilized for SFD

The SFD is effective on the same partial annular geometry given in Figure 3.9 on both sides of the pendulum. A schematic representation of cross-sectional view of the mechanical sensing core assembly is given in Figure 3.10.

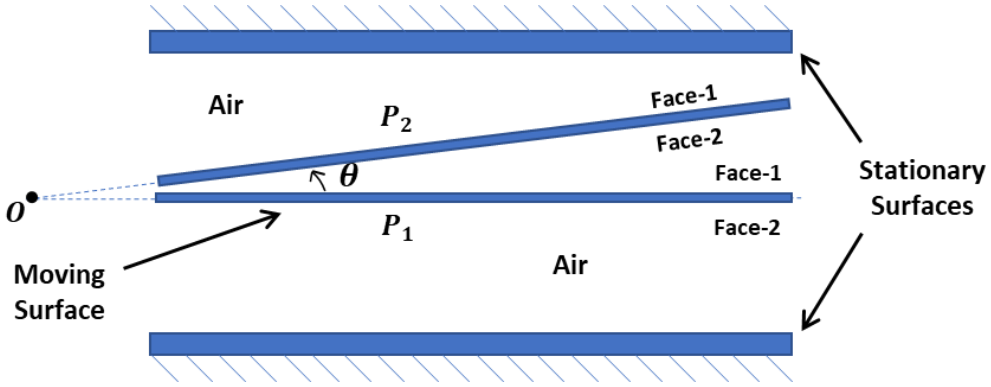

Figure 3.10. Schematic Representation of the Cross Sectional View of Mechanical Sensing Core Assembly

In Figure 3.10, stationary surfaces represent magnetic case surfaces, moving surface represents the annular plate that SFD takes place, P_1 and P_2 are two different positions of the annular plate. Squeeze film effects take place on both sides of the pendulum, which are named Face-1 and Face-2. Since single degree of freedom rotational system assumption is made for pendulum, annular plate is rotating about point O, where θ is same deflection angle. Amplitude and distribution of the pressure due to SFD depend on the air gap between moving and stationary surfaces. Therefore, $F_{SFD}(\theta)$ and $l_{SFD}(\theta)$ are different at positions P_1 and P_2, even if directions and amplitudes of the velocities of the pendulum are same. SFD is modelled for θ values from 0 to 1.2 mrad.

Before modelling, rarefaction phenomenon, compressibility phenomenon, border effects and amplitude effects are investigated for the structure as below;

- **Rarefaction Phenomenon:** At low ambient pressures viscosity of the gas decreases and squeeze film damping effect reduces [26–30]. In such cases viscosity is replaced by effective viscosity which is dependent on Knudsen number, given in Equation (3.20):

$$K_n = \lambda / h_0 \tag{3.20}$$

  where λ is mean free path of molecules and h_0 is the nominal air film thickness. At the ambient conditions the mean free path λ_0 of the air is

$0.064\mu m$. The air gap in the system investigated in this study is large compared to this value and system works in atmospheric pressure conditions. In result, K_n for the system is smaller than 0.01 and rarefaction effects are negligible [15]. Therefore, dynamic viscosity of the air at room temperature and atmospheric pressure is used in material model of the gas in the system.

- **Compressibility Phenomenon:** Compressibility of the gas in between gap is another important parameter in modelling of squeeze film effects. The squeeze number, σ, is introduced in Equation (3.21) to investigate compressibility where μ is the viscosity of the gas, ω is the radial frequency of the motion, l is the typical length of the plate and P_a is the ambient pressure.

$$\sigma = \frac{12\mu\omega l^2}{P_a h_0^2} \tag{3.21}$$

When the squeeze number is small, gas in between gap can be assumed as incompressible since it can flow out without compression during motion of the plate. However, with the increase of squeeze number compressibility of the gas cannot be neglected. Compressibility effects become significant when oscillations have high frequency or when the lateral dimension to film thickness ratio is high. This leads to a spring like behavior by gas which may affect dynamics of the system in a negative manner. Compressibility is negligible for $\sigma << 1$ [15]. The requirement of the dynamic frequency range for the specifically investigated product is up to 2000 Hz. The squeeze number is less than 0.2 for interested maximum amount of displacement of the pendulum and maximum input frequency. Therefore, compressibility effects and elastic force due to squeeze film effects are neglected in this study and squeeze film effects are modelled only as a damping source.

- **Border Effects:** Most of the analytical modelling approaches on squeeze film effects assume zero relative pressure on borders of the moving plate. This assumption is accurate for the systems with the ratio of high lateral

dimension to air gap thickness [14], which is also valid for the structure analyzed in this study. Therefore, border effects are neglected in this study and vanishing relative pressure on borders is assumed as the boundary condition of SFD model.

- **Amplitude Effects:** Deflections with small amplitude make possible to use of linearized Reynolds equation in continuum region. Sadd and Stiffer [28] analyzed effects of motion with large amplitudes for small squeeze number. Equation (3.22) is used to calculate a correction parameter, $f_d(\epsilon)$, for large amplitudes and recalculate damping coefficient by simply multiplying it by correction parameter.

$$f_d(\epsilon) = \frac{1}{(1-\epsilon^2)^{3/2}} \tag{3.22}$$

  where displacement ratio is $\epsilon = h/h_0$, h and h_0 are displacement of the moving surface and nominal air gap between moving and stationary surfaces. In this study, pendulum makes a rotational motion instead of translational motion. Translational damping coefficient and geometrical location of the pressure distribution due to squeeze film effects are obtained corresponding to different angular displacements by FEA to include amplitude effects in modelling of SFD.

Thin-Film Flow module of the software package COMSOL Multiphysics® [45] is used to model and analyze squeeze film effects on the surface given in Figure 3.9. Moving surface is modelled in 2D and meshed geometry is given in Figure 3.11. Two stationary surfaces are defined below and above moving surface which represent the capacitive surfaces on magnetic cases along each side of the pendulum. Simple schematic of the cross-sectional view of the analysis model is given in Figure 3.10. To obtain rotational damping coefficient, $C_r(\theta)$ as a function of rotational displacement θ, two stationary surfaces are defined parametrically as a function of θ. Gas medium is modelled as ambient air at room temperature and atmospheric pressure. Modified Reynolds equation is used to model interaction between gas,

stationary and moving surfaces. The boundary conditions for this model are vanishing relative pressure at the border of the plate. Moving surface is assumed to move rigidly only along surface normal direction, pointing out of the paper with a prescribed sinusoidal velocity. Parametric sweep analysis is done in frequency domain with small amplitude motion assumption. Results are obtained for θ values from 0 to 1.2 mrad. On the other hand, analyses are done for frequencies of motion as 100Hz, 500Hz, 1000Hz and 2000Hz to observe effects of different frequencies on damping.

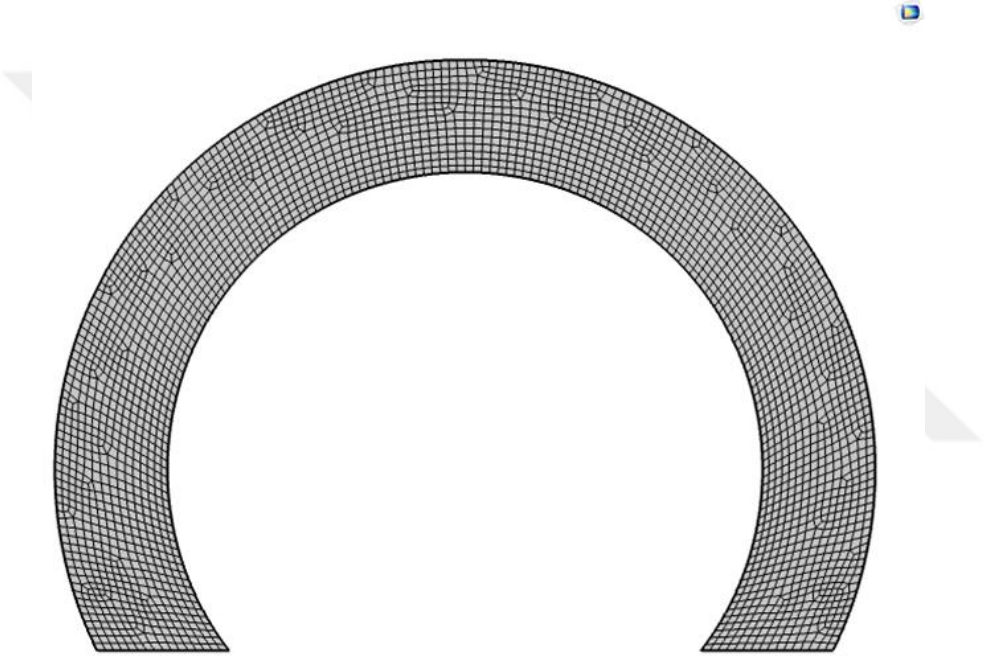

Figure 3.11. Mesh Structure of the Partial Annular Plate

It is observed that the motion of the moving plate causes squeeze film effects on both sides of it. When plate moves through top stationary surface, positive pressure develops on Face-1 and negative pressure develops on Face-2. The total force on the moving plate is equal to the sum of the forces acting on these two surfaces. In Figure 3.12 pressure distributions on both faces for two different values of θ are given.

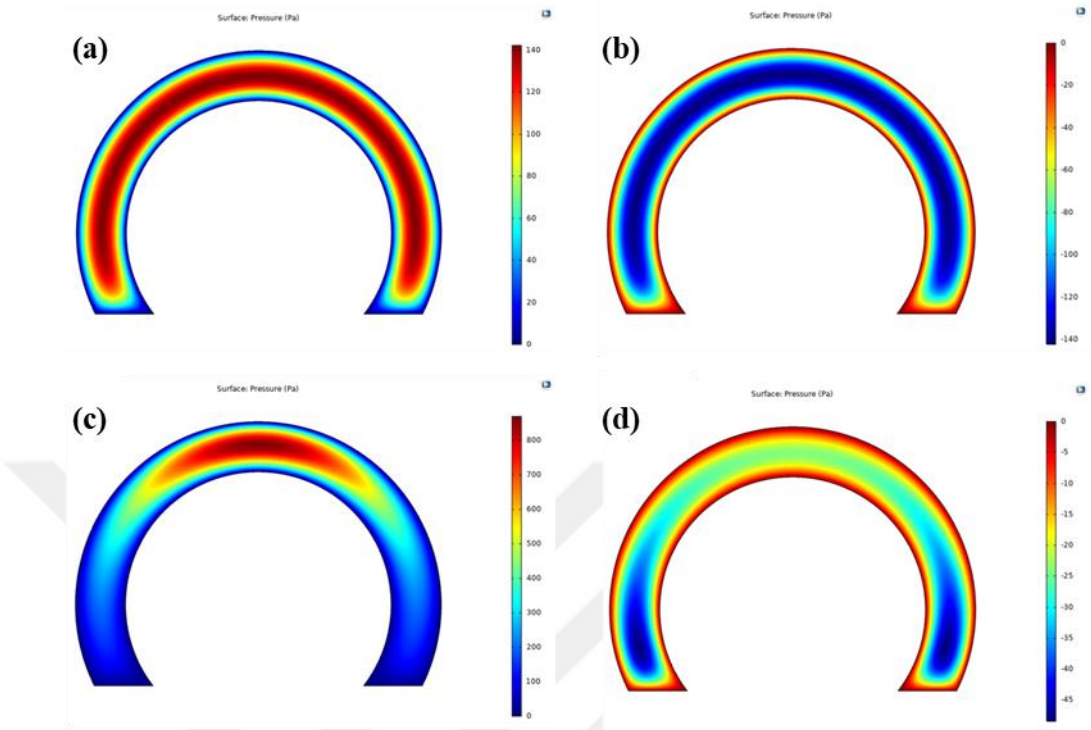

Figure 3.12. (a) Pressure Distribution on Face-1 at Position P_1, (b) Pressure Distribution on Face-2 at Position P_1, (c) Pressure Distribution on Face-1 at Position P_2, (d) Pressure Distribution on Face-2 at Position P_2

As it can be seen in Figure 3.12, pressure distribution, its amplitude and therefore geometrical center change with amount of deflection. For the case P_1, θ being equal to zero, the pressure is zero along the border and it increases towards the center of the surface. Absolute value of the pressure distribution is same for Face-1 and Face-2. For the case P_2, θ is larger than 0, and therefore, the distance between moving and stationary surfaces are not constant along the surface. Therefore, the pressure on Face-1 increases towards tip of the pendulum and it becomes dominant in comparison to pressure on Face-2.

On the other hand, numerical values of pressure distribution and translational damping coefficients are obtained from analysis results. Geometrical center of pressure due to squeeze film effects for each value of θ is calculated and therefore,

the location of damping force for each value of θ is obtained. Then, rotational damping coefficient $C_r(\theta)$ is calculated for θ values of 0 to 1.2 mrad using equation (3) which is given in Figure 3.13.

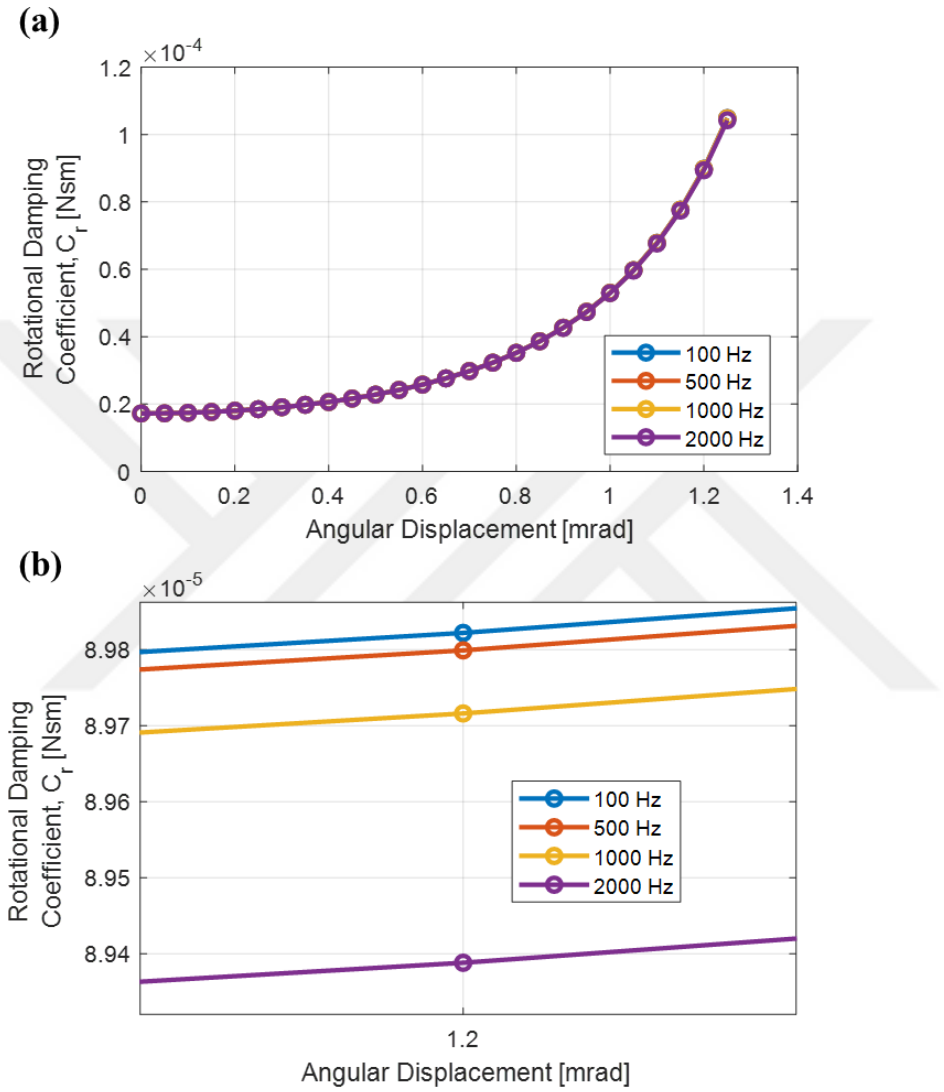

Figure 3.13. (a) Rotational Damping Coefficient vs Angular Displacement for Motions with Different Frequencies, (b) Rotational Damping Coefficients for 1.2mrad Angular Displacement and for Motions with Different Frequencies

Due to design parameters, $C_r(\theta)$ changes less than 1% between motion frequencies with 100Hz and 2000Hz. Therefore, effects of frequency of the motion are neglected

for further calculations. A polynomial function is fitted to the data obtained for motion with 100Hz frequency to be used later in system level models.

3.4 Modelling of Magnetic Feedback Torquer

Magnetic feedback torquer is used to provide a rebalance force against inertial force in a closed loop manner when accelerometer exposed to acceleration. Top view and cross-sectional view of magnetic feedback torquer component is given in Figure 3.14.

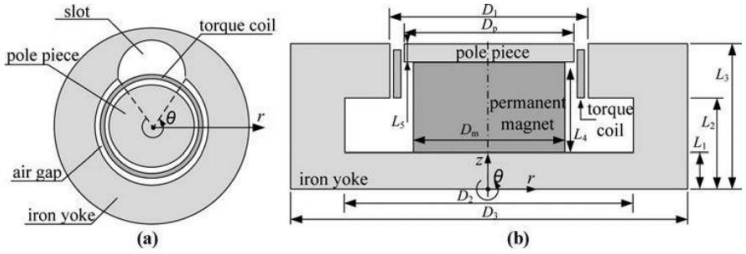

Notes: (a) Top view; (b) enlarged sectional view with labeled dimensions

Figure 3.14. Top and Cross-Sectional View of Magnetic Feedback Torquer [46]

Torquer coil on quartz plate-coils assembly is in air gap of the magnetic case assembly, as it is shown in Figure 3.14. The magnetic flux flows out from the permanent magnet which serves as a magnetic flux source and returns to the magnet through the magnetic case. Therefore, there is always magnetic flux density on torquer coil. Current flow through torquer coils causes magnetic force named as Lorentz force which can be given as:

$$F_m(I) = 2BIl_c \tag{3.23}$$

where B, l_c and I denotes magnetic flux density on each coil, length of each coil and current flow through coils. Note that $F_m(I)$ defines magnetic force on two coils in total. Value of B is obtained experimentally to be used in the model. Forces acting on pendulum under a static acceleration load at steady state is given in Figure 3.15.

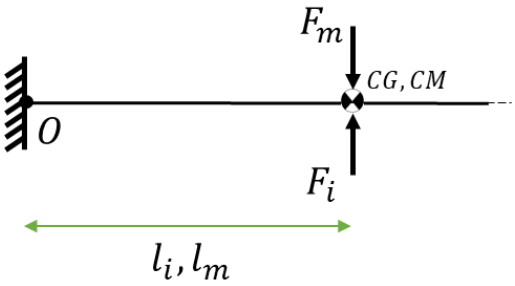

Figure 3.15. Forces Acting on Pendulum Under a Static Acceleration Load at Steady State (*Coils are not shown*)

Since CG and CM are identical in an ideal design, l_i and l_m are equal. Therefore, it is assumed that inertial force is equal to magnetic force in steady state. B can be calculated by using equality of Equation (3.4) and (3.23).

$$B = \frac{ma_i}{2Il_c} \tag{3.24}$$

Acceleration output of the sensor is obtained as a potential difference, V_L, by using load resistor, R_L. Therefore, Equation (3.24) is modified as follows.

$$B = \frac{ma_i}{2\left(\frac{V_L}{R_L}\right)l_c} \tag{3.25}$$

V_L is obtained by accelerometer when input acceleration a_i is equal to gravitational acceleration. Since values of m, R_L and l_c are known by design, B is obtained by using Equation(3.25).

3.5 Modelling of Sensor Electronics

Sensor electronics are mainly comprised of capacitive pickoff demodulator and controller circuits. Capacitive pickoff is used to sense displacement of the pendulum. Displacement of the pendulum causes the capacitive inequality in the system as it is given in Figure 3.3.

Capacitance value of a parallel plate capacitor is given in Equation (3.26).

$$C = \epsilon \frac{A}{d} \tag{3.26}$$

where ϵ, A and d are dielectric permittivity of the medium in between capacitor terminals, surface area of the capacitive surfaces and distance between capacitive surfaces. Relation between pendulum displacement and capacitance is not linear since d is in the denominator of the equation. Moreover, the pendulum in the accelerometer is a rotational system, which means it does not move translationally. This makes relation between pendulum displacement and capacitance more nonlinear. Relation between capacitive pickoff output signal and displacement of pendulum is given in Equation (3.27).

$$V_{po} = \theta K_{po}(\theta) \tag{3.27}$$

where V_{po} and $K_{po}(\theta)$ is capacitive pickoff output signal and capacitive pickoff gain. Capacitive pickoff gain $K_{po}(\theta)$ is modelled as displacement dependent because of nonlinear characteristics of the capacitance change. It is obtained by experimental results of open loop tests, which is described in detail in Section 4.2.2.

Capacitive pickoff output signal, V_{po}, is fed to the controller. The output of the controller, V_c, is used to supply feedback current which flows through torquer coils to generate magnetic feedback force on pendulum. Controller in the system is modelled as a PID controller. Relation between capacitive pickoff output signal and output of the controller in time domain is given in Equation (3.28).

$$V_c(t) = K_P V_{po}(t) + K_i \int^t V_{po}(t)dt + K_d \frac{dV_{po}(t)}{dt} \tag{3.28}$$

where K_p, K_i and K_d are proportional, integral and derivative constants of the controller.

3.6 Modelling of Torquer Coils and Readout Circuit

QFA gives current that flows through torquer coils to the outside of the accelerometer. A load resistor is used at the outside of the accelerometer as a readout circuit to obtain acceleration information in voltages. An electronical schematic representation of torquer coils and readout circuit is given in Figure 3.16.

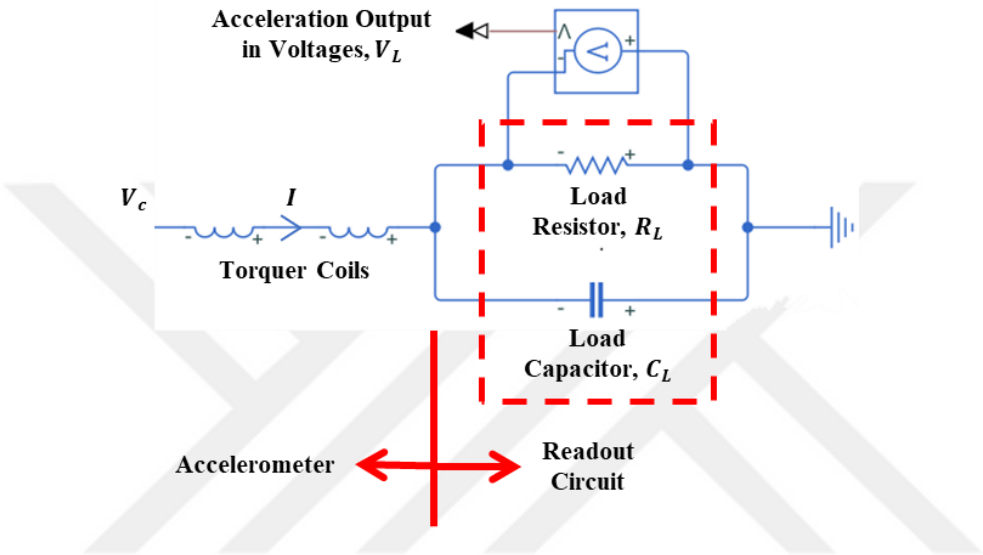

Figure 3.16. Schematic Representation of Torquer Coils and Readout Circuit

Since the sensor is a closed-loop system, the current passing through the coils per unit acceleration does not change with change in R_L. Additionally, as the R_L increases, V_L per unit acceleration and resolution increase. However, since the sensor is powered by a specific power level, the electronic circuit saturates at higher acceleration levels. This limits the maximum current that can be generated, even if more current is necessary for the closed-loop system under high acceleration loads. This electronic saturation consequently determines the measurement range of the sensor, where a decrease in R_L leads to an increase in the measurement range. Relations between R_L, maximum measurement range and V_L per gravitational acceleration are given in Figure 3.17:

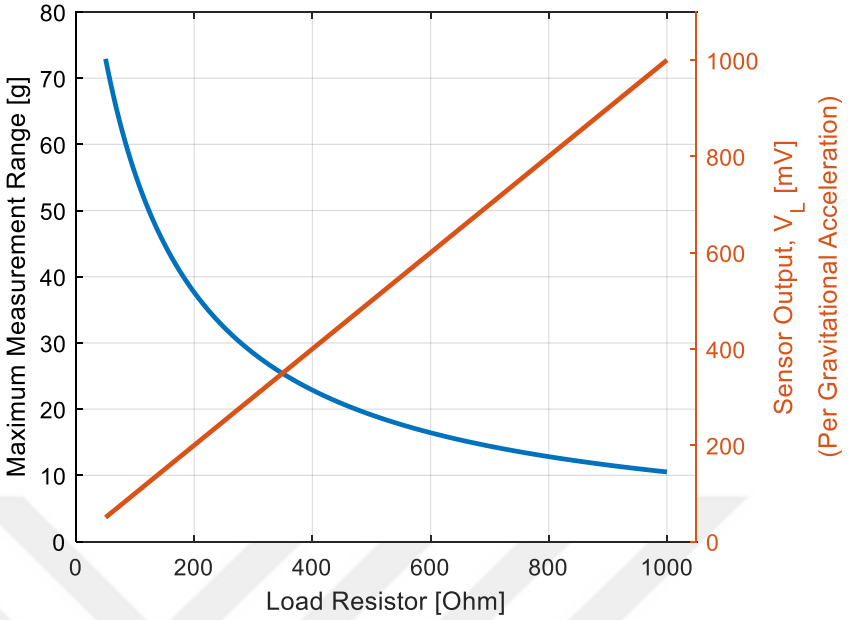

Figure 3.17. Relation Between R_L, Maximum Measurement Range and V_L per Gravitational Acceleration

R_L is a parameter in the closed loop system, therefore it directly affects the dynamic response of the system. A capacitor named as load capacitor, C_L, can be used together with R_L to filter sensor output as it is shown in Figure 3.16. Özmen et al. [47] characterize QFA and readout circuit by using identification methods and investigate effects of R_L and C_L on experimental results. Relations between V_C and I is given in Equation (3.29), relation between I and V_L is given in Equation (3.30) in s domain.

$$I(s) = \left(\frac{sR_LC_L}{s^2R_LC_LL_t + s(R_LC_LR_t) + (R_t + R_L)}\right)V_c(s) \tag{3.29}$$

$$V_L(t) = \left(\frac{R_L}{sR_LC_L + 1}\right)I(s) \tag{3.30}$$

where R_t and L_t are total resistance and total inductance of two coils.

3.7 Conclusions

In this section, first, QFA is introduced by giving detailed information about all mechanical and electronical components of it. Components in the system and working principles are described in detail. Each component in the system is then modelled by analytical calculations, FEA, or experiments in order to use in the system level models. Pendulum is modelled as a single degree of freedom rotational system. Rotational stiffness constant is obtained by simple analytical calculations and inertia is obtained from CAD model. On the other hand, effects of SFD changes as pendulum displaces. Therefore, rotational damping coefficient is modelled by FEM as displacement dependent. Magnetic feedback force is modelled as Lorentz force, where it is assumed that magnetic force on the pendulum is equal to inertial force and thus magnetic flux density is obtained experimentally. Controller and readout circuit are modelled analytically.

CHAPTER 4

MODELLING OF QUARTZ FLEXIBLE TYPE ACCELEROMETER AS OPEN AND CLOSED LOOP SYSTEMS

4.1 Introduction

In this section, QFA is modelled both as open loop and closed loop systems. Block diagram representations of both models are given. The prototype working in an open loop manner comprised of mechanical sensing core assembly and modified sensor electronics is used in open loop model verification experiments. They consist of step response tests against different inputs. Capacitive pickoff gain, $K_{po}(\theta)$, is also characterized by using test results. The closed loop system model is verified by using the prototype comprised of mechanical sensing core assembly and sensor electronics including controller. Experimental verification of the closed loop system model includes sine sweep and shock tests to obtain input-output frequency response and shock response of the accelerometer.

4.2 Modelling of the Quartz Flexible Accelerometer as an Open Loop System

Within the closed-loop system, a controller is utilized to automatically maintain the pendulum at its nominal position. In the open-loop system, however, there is no controller used; the coils are driven manually, allowing for the alteration of the position. To observe accuracy of the displacement dependent damping model, step responses of the open loop system to the different levels of external current excitations are investigated. On the other hand, capacitive pickoff gain, $K_{po}(\theta)$, is characterized by steady state response of the open loop test prototype to the different magnetic force inputs. Sensor electronics is modified and mechanical sensing core

assembly is used with sensor electronics without controller. The modified open loop working system is given schematically in Figure 4.1.

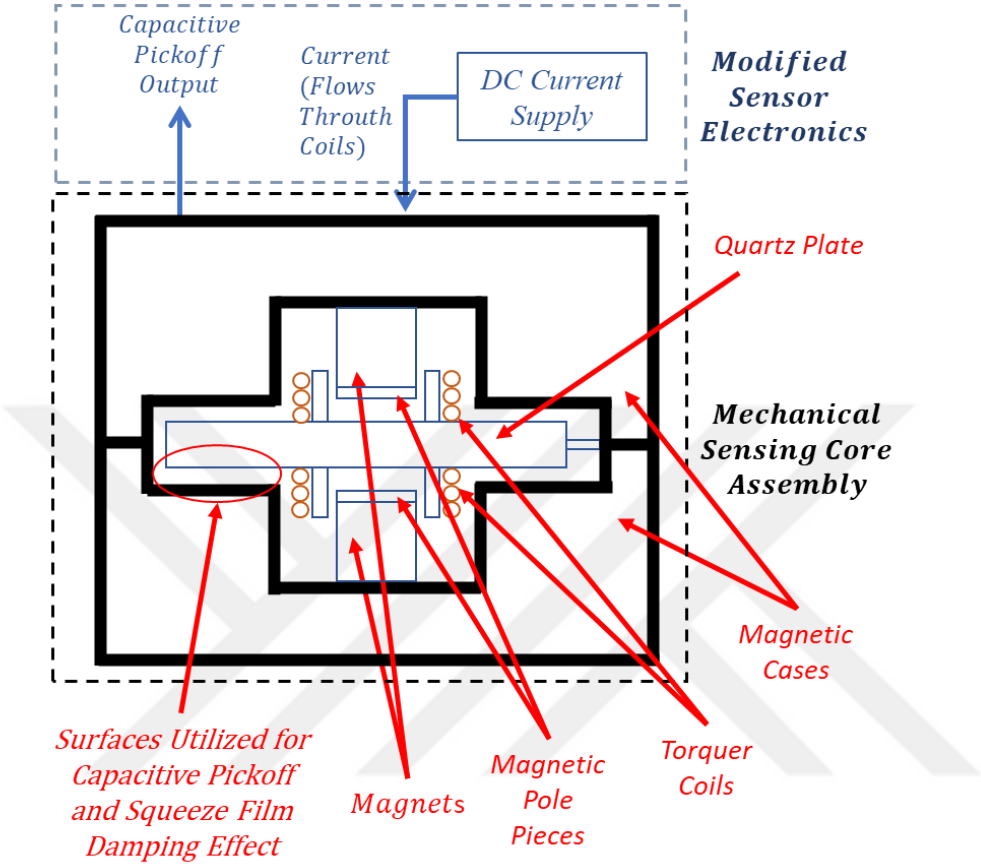

Figure 4.1. Schematic Representation of the Open Loop Accelerometer

4.2.1 Block Diagram Representation of the Quartz Flexible Accelerometer as an Open Loop System

To work in an open loop manner, controller is not used in the model. Magnetic feedback torquer structure is excited externally by predefined current input to the torquer coils. Output of the capacitive pickoff signal from the demodulator is obtained as voltage and converted to angular displacement. Block diagram representation is given in Figure 4.2.

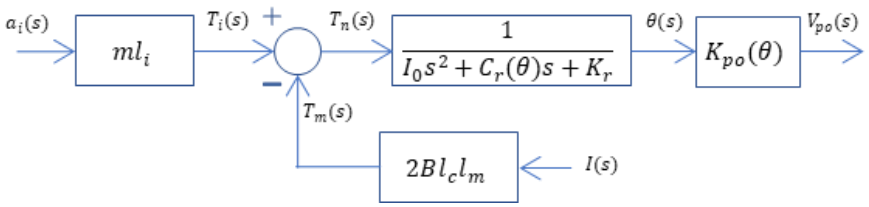

Figure 4.2. Block Diagram of the Accelerometer as an Open Loop System

where $a_i(s)$, $I(s)$, $T_i(s)$, $T_m(s)$, $T_n(s)$, $\theta(s)$, V_{po} represents exposed acceleration (input acceleration to the system), externally supplied current to the coils, torque due to inertial force, torque due to magnetic force, net torque on the pendulum, angular displacement and output of the capacitive pickoff respectively. $K_{po}(\theta)$ is the gain of the capacitive pickoff, which defines relation between angular displacement and electronic output of the pickoff demodulator in the sensor electronics. This parameter is not a constant gain and depends on instantaneous angular displacement since relation between $V_{po}(s)$ and $\theta(s)$ is not linear. $C_r(\theta)$ in the model depends on instantaneous angular displacement. Software package MATLAB® [48] and SIMULINK® [49] is used to run simulations. SIMULINK® model is given in Figure 4.3:

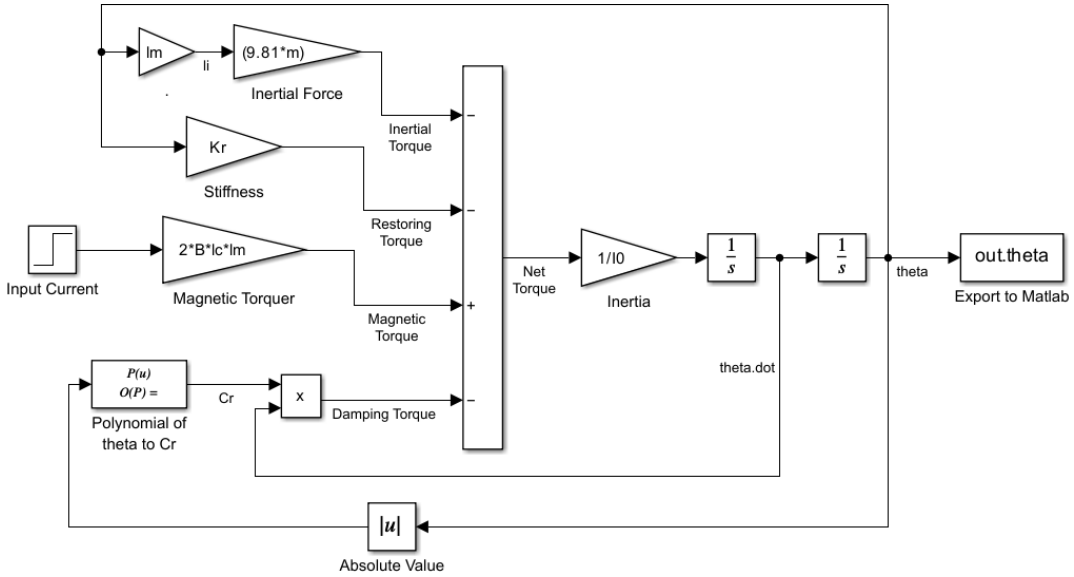

Figure 4.3. SIMULINK® Model of Open Loop System

SIMULINK® model given in Figure 4.3 give displacement θ as a result of input current flows through coils I. Step type input is used for input current. The model is not a linear time invariant model since rotational damping coefficient $C_r(\theta)$ is updated in each step of the simulation dependent on θ. The model is run from a MATLAB® script and output of it is exported to the MATLAB® again. Different cases are observed for different initial conditions and input amplitudes. Schematic representations of pendulum are given Figure 4.4 which shows different cases examined:

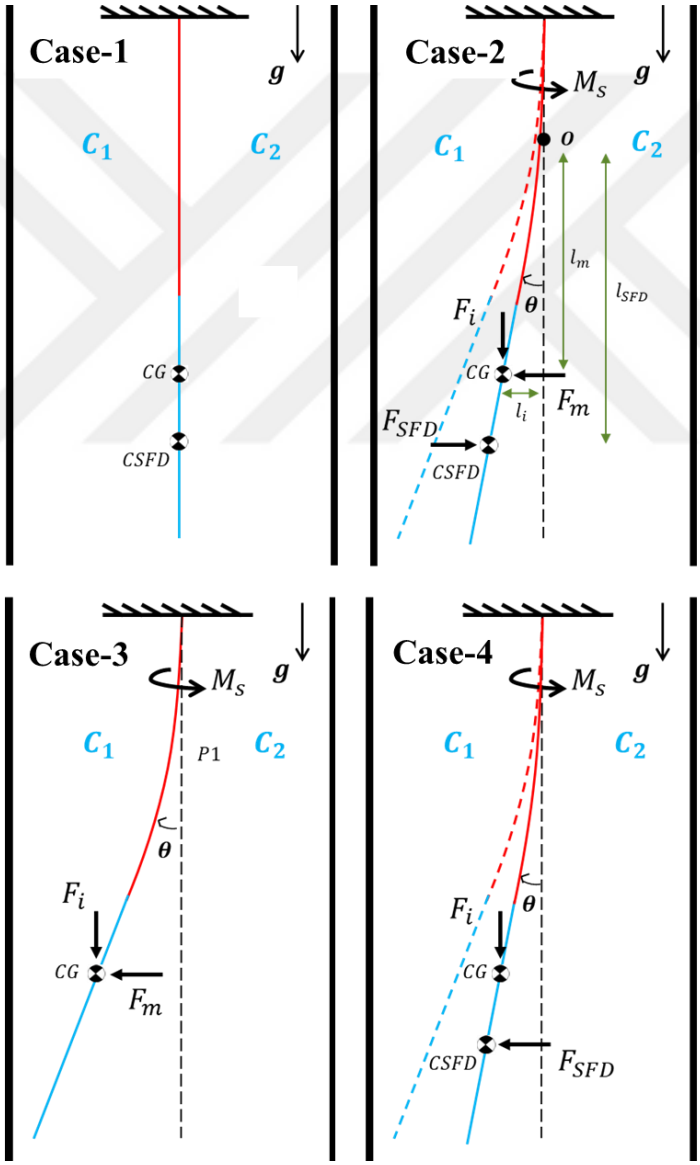

Figure 4.4. Investigated Cases for Open Loop System

Forces acting on pendulum for four different cases of pendulum are given in Figure 4.4. C_1 and C_2 are the capacitance of the capacitors of the capacitive pickoff and those aforementioned cases briefly are;

- **Case-1:** This is the static equilibrium position where $C_1 - C_2 = 0$, there is no external coil excitation and therefore no magnetic force on pendulum.
- **Case-2:** This is the transient step response to the magnetic force F_m. Motion is from Case-1 to Case-3. Initial condition is Case-1 for this case.
- **Case-3:** This is the static equilibrium position where constant external coil excitation and therefore constant magnetic force F_m, constant inertial force and constant recovery spring torque exist on pendulum.
- **Case-4:** This is the transient step response since magnetic force F_m vanishes instantaneously. Motion is from Case-3 to Case-1. Initial condition is Case-3 for this case.

In the above procedure, Case-1 and Case-3 determine the initial conditions for θ, F_m and F_i. Case-2 and Case-4 are the main cases of the investigations to obtain step responses of the open loop system. Simulations are done for 12 different amplitudes of the excitation signal, $I = (1,2,3 \dots 12)mA$. For $I = 12mA$ maximum amount of amplitude ratio is 83% at tip of the plate and minimum amount of amplitude ratio is 9%. Results are used for two main objectives. First, by using steady state θ values from simulations and steady state $V_{po}(\theta)$ values from open loop test results, capacitive pickoff gain $K_{po}(\theta)$ is modelled. Second, transient responses to the step inputs are compared to verify open loop system model.

4.2.2 Characterization and Verification Experiments of the Open Loop System Model of the Quartz Flexible Accelerometer

The sensor electronics of the tested prototype is modified and the controller in it is suspended to obtain an accelerometer working in an open loop manner. Equipment of open loop test setup are given in Figure 4.5:

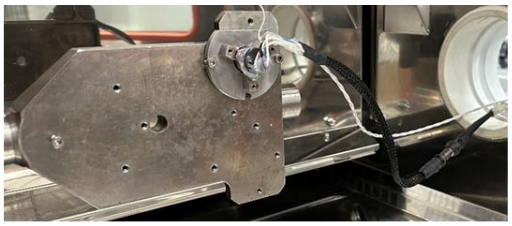

Single Axis Rotating Table, Test Prototype

LMS Data Acquisiton System

DC Current/Voltage Source

Power Supply

Figure 4.5. Equipment of the Open Loop Test Setup

The test prototype is mounted on a single axis rotating table. The rotating table allows for the orientation adjustment of the prototype, enabling the nullification of the gravitational force effect on the pendulum along sensitive direction and it is used to set orientation of the pendulum as in Case-1 given in Figure 4.4, prior to start experiments. Input current to the coils is provided using the DC current/voltage source. LMS data acquisition system is used to collect output of the capacitive pickoff, V_{po}, of the test prototype. Test data is gathered with sampling frequency of 10 kHz.

As it is done for simulations, experiments are conducted for excitation signals with 12 different amplitudes. Step responses of the open loop test prototype during Case-2 and Case-4 are obtained for input amplitudes $I = (1,2,3 \dots 12)mA$. By using steady state θ values from simulations and corresponding steady state $V_{po}(\theta)$ values from open loop tests of Case-2, relation between θ and $V_{po}(\theta)$ is obtained and shown in Figure 4.6:

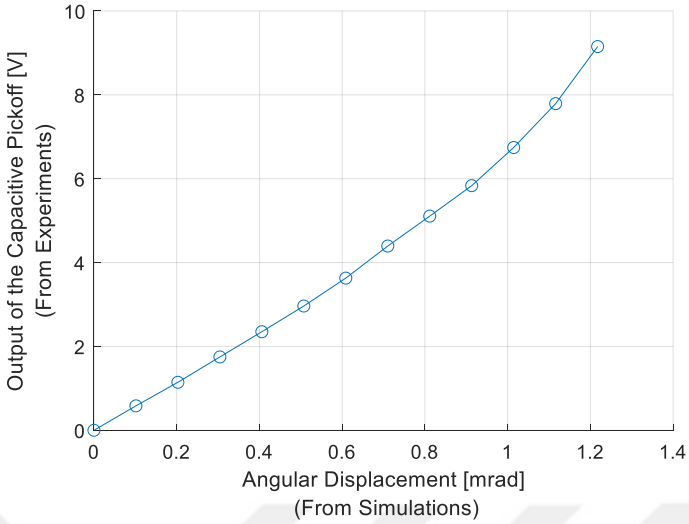

Figure 4.6. Relation Between θ and V_{po}

A polynomial function is fitted to the data in Figure 4.6 and capacitive pickoff gain, $K_{po}(\theta)$, is obtained experimentally. Then, obtained $K_{po}(\theta)$ is used to convert results of experiments, $V_{po}(\theta)$ to θ. Transient step responses for Case-2 and Case-4 by simulations and experiments are given in Figure 4.7-Figure 4.10. Figures are given for only minimum and maximum displacement conditions for simplicity:

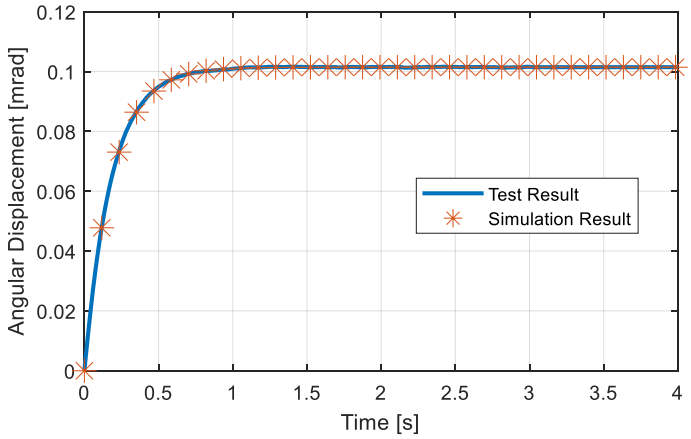

Figure 4.7. Step Responses by Simulations and Tests, $1\mu A$ excitation for Case-2

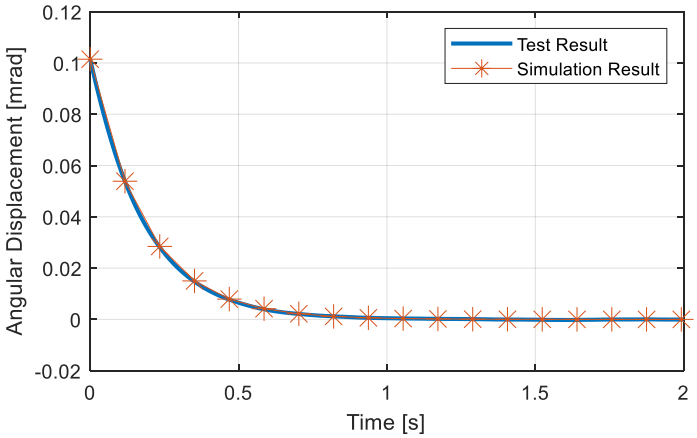

Figure 4.8. Step Responses by Simulations and Tests, $1\mu A$ excitation for Case-4

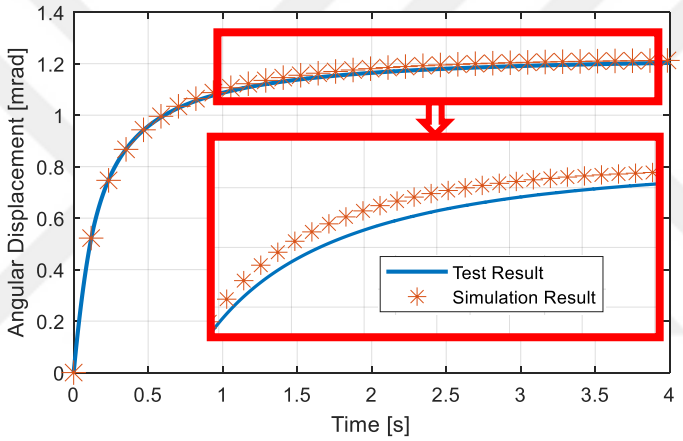

Figure 4.9. Step Responses by Simulations and Tests, $12\mu A$ excitation for Case-2

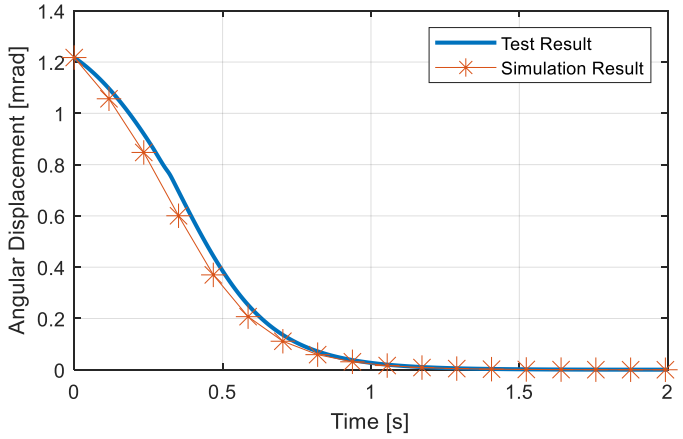

Figure 4.10. Step Responses by Simulations and Tests, $12\mu A$ excitation for Case-4

Settling time of each step response from simulations and experimental results are obtained to make a comparison between them. For Case-2 98% of steady state value and for Case-4 2% of initial value are used to determine settling times. Percentage difference between simulation and experiment is calculated as:

$$dif_{ts} = \frac{ts_{sim}^{pos} - ts_{exp}^{pos}}{ts_{sim}^{pos}} * 100 \quad (4.1)$$

where ts_{sim}^{pos} is settling time of simulation and ts_{exp}^{pos} is settling time of experimental result. Percentage differences between settling times of simulations and experiments are given in Table 4.1:

Table 4.1 Percentage Differences Between Settling Times of Simulations and Experiments

	Torquer Current (μA)											
	1	**2**	**3**	**4**	**5**	**6**	**7**	**8**	**9**	**10**	**11**	**12**
$\boldsymbol{dif_{ts}^{Case-2}}$ **(%)**	-0.2	1.8	3.0	4.0	5.2	5.0	5.9	5.6	4.2	0.6	-8.2	-31.7
$\boldsymbol{dif_{ts}^{Case-4}}$**(%)**	0.3	0.8	0.3	0.8	0.5	1.5	1.6	1.9	2.0	2.0	0.8	-3.7

Results are in a high level of agreement for low amplitudes. As deflection of the pendulum increases, it is observed that the difference between numerical and experimental results increases. dif_{ts}(%) results are less than 6% for amplitude ratios at the tip of the pendulum under 50%.

4.3 Modelling of the Quartz Flexible Accelerometer as a Closed Loop System

QFA is a force rebalance type accelerometer, so it has a controller and it works in a closed loop manner. To examine the dynamic performance of the accelerometer, it needs to be modeled as a closed-loop system comprised of all components in it. For

this purpose, the closed-loop model of the sensor is being modelled and verified by experiments including sine sweep and shock tests.

4.3.1 Block Diagram Representation of the Quartz Flexible Accelerometer as a Closed Loop System

Block diagram of a single axis non-gyroscopic closed loop accelerometer is given in [43]. Block diagram used in this study for the system includes accelerometer and readout circuit is given in Figure 4.11:

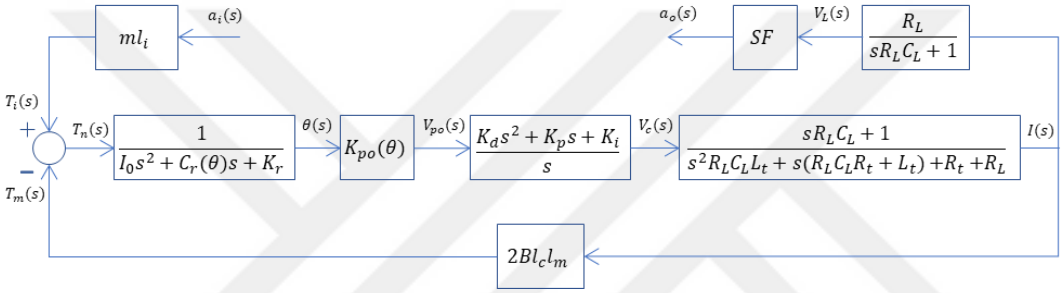

Figure 4.11. Block Diagram of the Accelerometer as a Closed Loop System

Readout circuit is included in the closed loop model since it has significant effects on system dynamics. $I(s)$, $V_L(s)$ and $a_o(s)$ represents controller output current, acceleration output of the accelerometer in terms of voltage and acceleration output of the accelerometer in terms of unit g. R_t, L_t, R_L, C_L and SF are resistance of coils, inductance of coils, resistance of the load resistor, capacitance of load capacitor and scale factor of the system correspondingly. Scale factor is simply used to convert accelerometer output to the desired unit. Software packages MATLAB® and SIMULINK® are used to run simulations. SIMULINK® model of the system is given in Figure 4.12 and Figure 4.13:

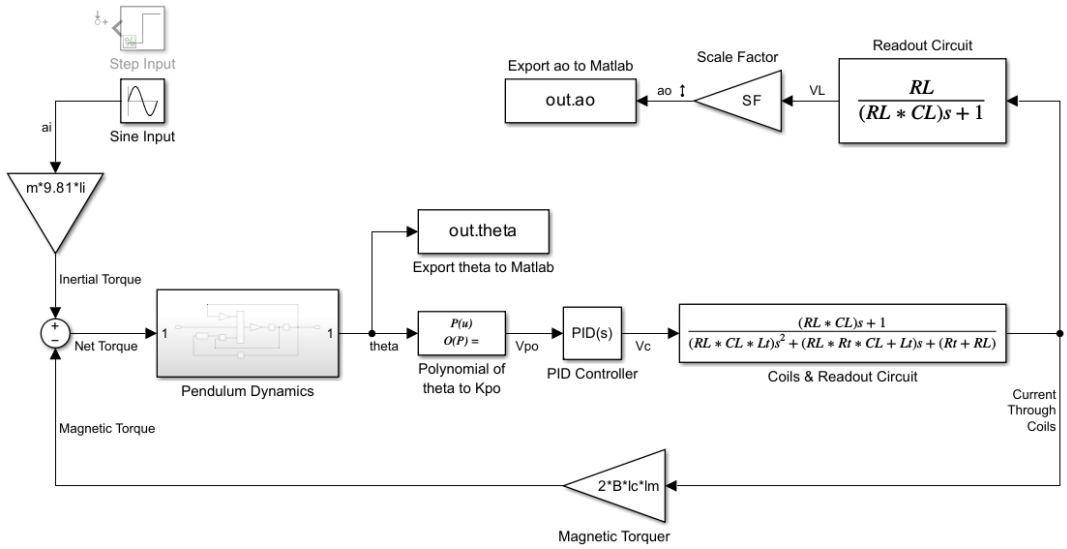

Figure 4.12. SIMULINK® Model of the Closed Loop System

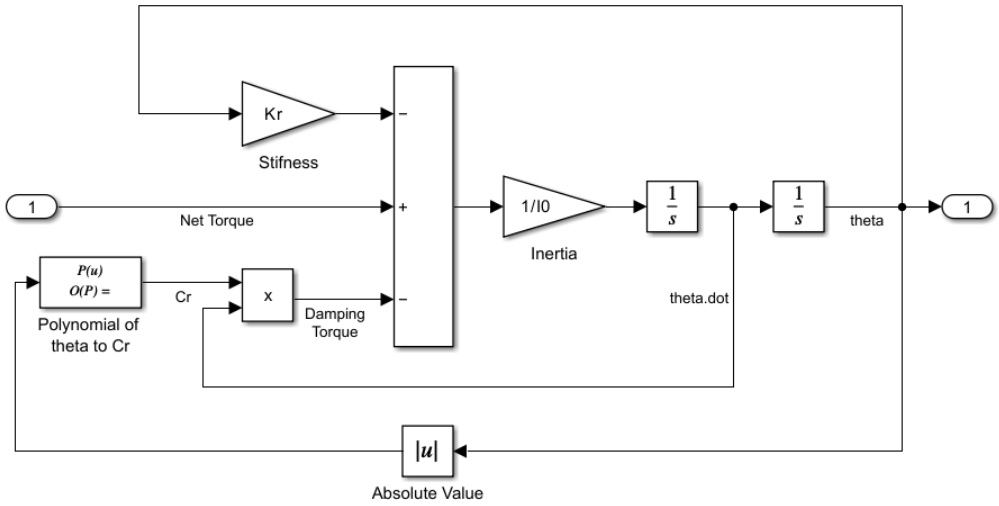

Figure 4.13. Pendulum Dynamics Subsystem Blocks in the SIMULINK® Model

The SIMULINK® model is used to examine various responses of the system in both time and frequency domains. Two of these are the acceleration input- acceleration output ($a_i(s)$-$a_o(s)$) and acceleration input-pendulum displacement ($a_i(s) - \theta(s)$) frequency responses of the system. The model is not a linear-time invariant model due to the displacement-dependent definitions of the $C_r(\theta)$ and $K_{po}(\theta)$ parameters. Therefore, built-in tools of the software cannot be utilized to obtain correct frequency response of the system. Instead, the SIMULINK® model is run within a loop using

a MATLAB® code. $\theta(s)$ and $a_o(s)$ values are stored in the MATLAB® environment as the model output. In each iteration of the loop, a sinusoidal signal with constant frequency is fed into the system as input for a specific duration. The total duration of the signal is determined to ensure the responses reach a steady state. The obtained simulation outputs and applied input signals are converted to the frequency domain using the FFT method. Output signals are divided by input signals and frequency responses are obtained as magnitude and phase values. This process is repeated using different frequencies of input signals to achieve the required resolution across the desired frequency range. Subsequently, by merging all the data, the desired frequency responses are obtained.

The same model is used to obtain responses of the system to the shock or step inputs in time domain.

4.3.2 Experimental Verification of the Closed Loop System Model of the Quartz Flexible Accelerometer

Sensor input-output frequency response is obtained from sine sweep tests and shock response is obtained from mechanical shock experiments. Mechanical shaker is used to excite system. Piezoelectric based accelerometers (PZT) with bandwidth values exceeding 10kHz are used to obtain reference acceleration values. Both force rebalance and piezoelectric based accelerometers are mounted on the same fixture, close to each other. Fixture is carefully designed to avoid resonance within the frequency range of interest (100-2000Hz). Equipment of closed loop test setup are given in Figure 4.14:

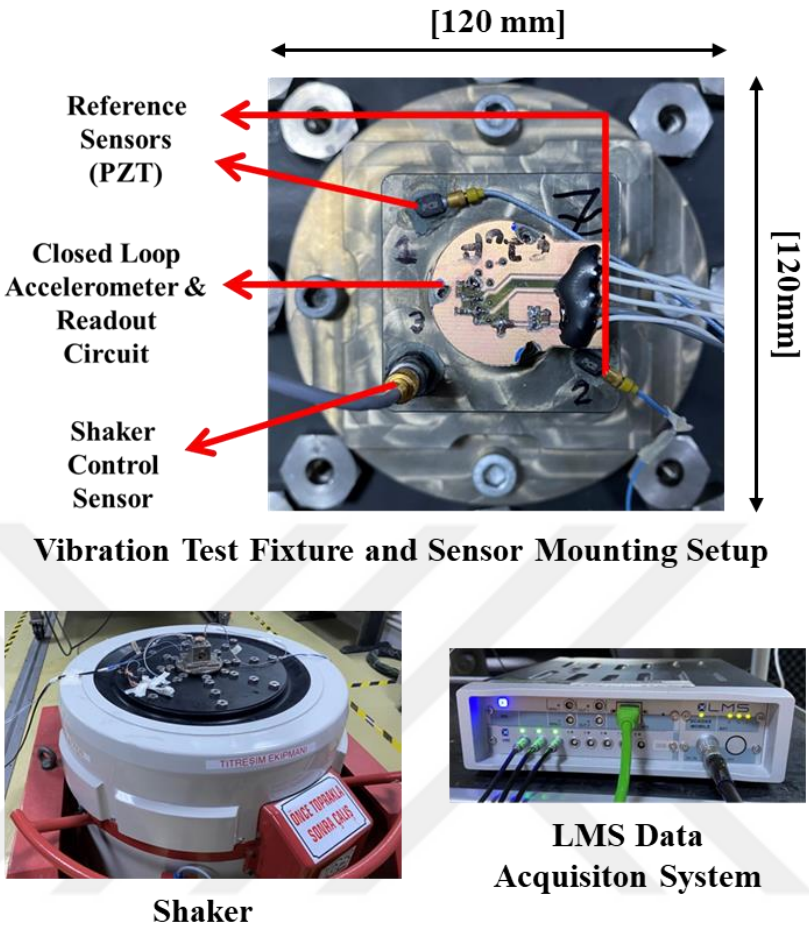

Figure 4.14. Equipment of the Closed Loop Test Setup

First, sinusoidal inputs with magnitudes of 3g and 10g are applied at a rate of 2 octave/minute within the frequency range of 100-2000Hz. Output of the QFA and output of the reference PZT accelerometers are then converted to the frequency domain using the FFT method. Data from QFA is divided by data from PZT and frequency responses are obtained as magnitude and phase values, which represent the acceleration input- acceleration output ($a_i(s)$-$a_o(s)$) frequency response of the system. Secondly, rectangular wave shocks with 5ms-3g and 5ms-10g amplitudes are applied to observe step response of the system where 5ms defines the duration of the shock and 3g and 5g defines the amplitude of it. Data is collected at a sampling rate of 102400 Hz through all tests. Input-output frequency responses and pendulum displacements are given in Figure 4.15 and Figure 4.16:

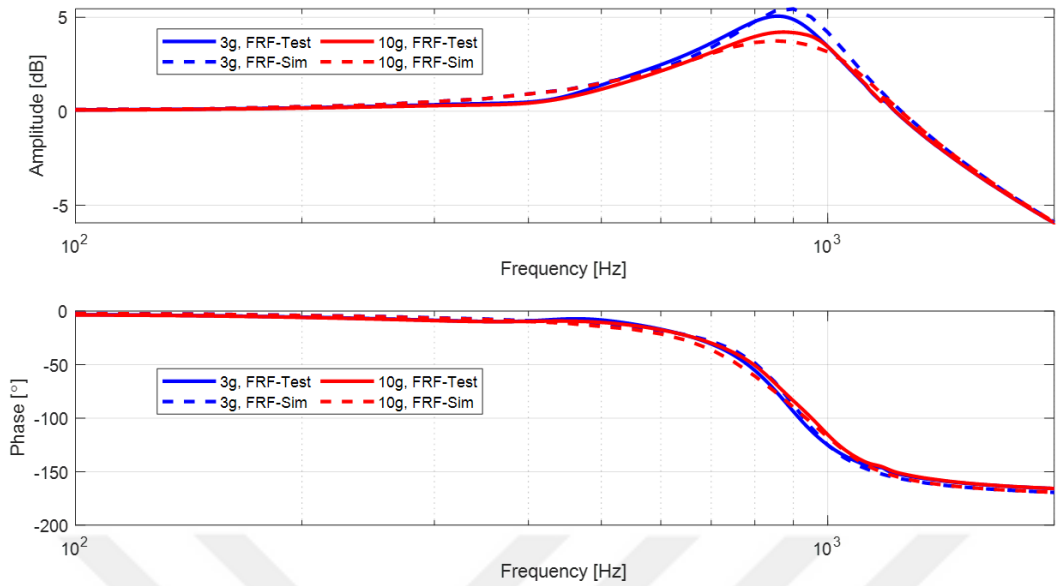

Figure 4.15. Sensor Input-Output Frequency Responses

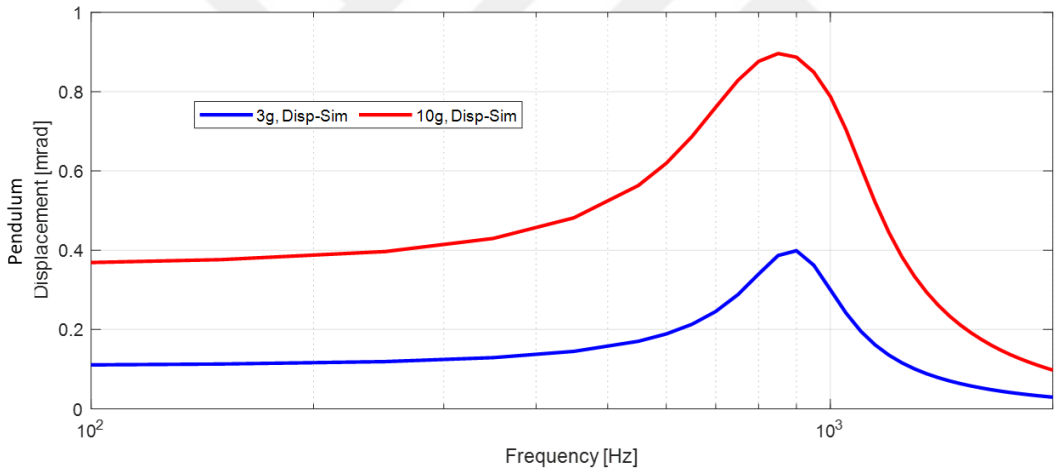

Figure 4.16. Frequency of Sensor Input-Amplitude of the Pendulum Displacement

"FRF-Test" and "FRF-Sim" in legend of the Figure 4.15 correspond to input-output frequency responses of the closed loop system from test and simulation. "Disp-Sim" in legend of the Figure 4.16 corresponds to amplitude of the sinusoidal pendulum displacement through input acceleration frequency obtained by simulations. Results are given for both 3g and 10g input acceleration amplitudes. The Accelerometer system has a resonance around 900Hz, which is obtained from the results of simulations. Pendulum displacement results are only obtained from simulations of

the closed loop system model. Displacement increases as amplitude of the input signal increases and amplitude of the system resonance is damped a certain amount. This phenomenon can be observed on experimental results since SFD is modelled as dependent on displacement. Shock responses of the system output and pendulum displacement to the rectangular wave shocks with 5ms-3g and 5ms-10g amplitude are given in Figure 4.17 and Figure 4.18:

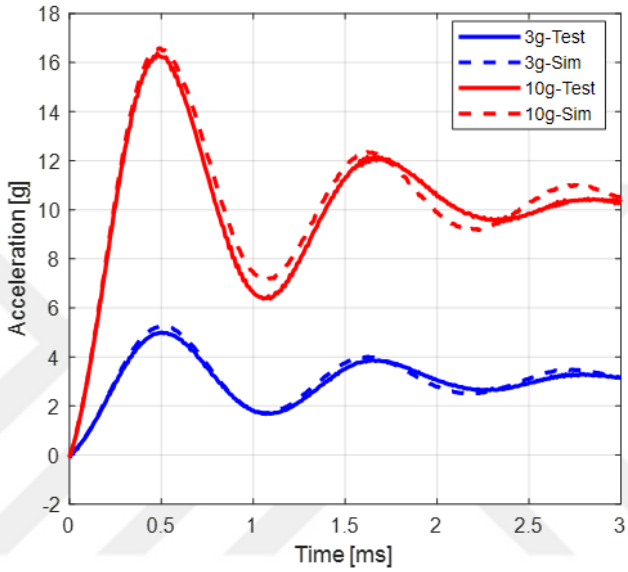

Figure 4.17. Mechanical Shock Responses of the Accelerometer

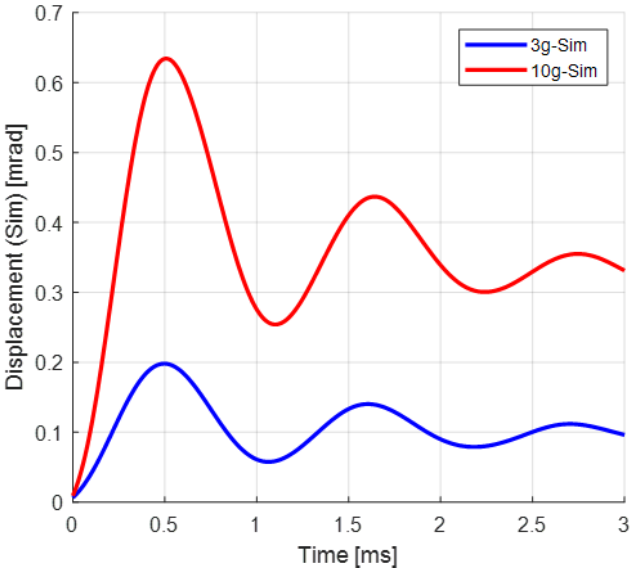

Figure 4.18. Pendulum Displacements During Shock Input

Difference between simulations and experimental results are less than 10% percent for both frequency response and shock response results.

4.4 Conclusions

In this section, first, accelerometer is investigated as an open loop system. Block diagram representation of the QFA as an open loop system is given. SIMULINK® model of the open loop system is provided which is used to obtain step response of the system. Then, experimental setup for characterization and verification is introduced. This setup is used to obtain responses of the open loop test prototype to step inputs with various amplitudes. Capacitive pickoff gain, $K_{po}(\theta)$, is characterized by test results dependent on displacement, θ. The results obtained from simulations and tests for open loop system are provided and it can be said that accuracy of the simulations is satisfactory for small displacements of the pendulum. Secondly, accelerometer is investigated as a closed loop system and the block diagram of it as a closed loop system is presented. SIMULINK® model of the closed loop system is given which is used to obtain frequency response and mechanical shock response of the system. Test setup used for the experimental verification of the closed loop system model is provided. Results from simulations and tests are presented for frequency response and mechanical shock response of the system. Maximum difference between the results from simulations and tests is calculated as less than 10% percent. The accuracy of the obtained closed loop system model is suitable for use in advanced-level design and optimization studies.

CHAPTER 5

SIMULATION BASED INVESTIGATION OF DESIGN REVISIONS ON PERFORMANCE OF QUARTZ FLEXIBLE ACCELEROMETER

5.1 Introduction

In this section, for the specific accelerometer prototype investigated in this study, effects of readout circuit and SFD on dynamic characteristics are obtained by simulations. Input-output frequency responses, input-pendulum displacement frequency responses and step responses of output of the accelerometer are investigated for different design parameters. Closed loop system model defined in Section 4.3.1 is used to perform simulations. Frequency responses are obtained for input accelerations with 1g amplitude and step responses are obtained for step input accelerations with 1g amplitude. Results are investigated in between 20-2000Hz in frequency domain and the performance criteria for obtained results are listed below:

- **Bandwidth of input-output frequency response is expected to be more than 400 Hz:** Bandwidth is the frequency that amplitude of the frequency response dropped to -3dB (half power) or phase difference dropped to -90° (delay of a ¼ period of sinusoidal signal). Navigation system bandwidth requirements are between 50-400Hz.
- **Bandwidth of input-output frequency response is expected to be less than 1000Hz:** Navigation systems are used and transported in moving vehicles such as land vehicles and aircrafts. MIL-STD-810 [50] provides guidelines and specifications for vibration testing, including methods for generating vibration profiles, test durations, frequencies and amplitudes. In this document, spectral densities of various vibrational loads are defined up to 2000Hz. Having an excessive bandwidth leads to the perception of high-frequency vibrational loads and adversely affects noise performance.

- **Input-pendulum displacement frequency response is expected to be resonance free:** Vibration rectification error (VRE) is a dynamic error, which defines the bias shift of mean of the sensor output under vibrational load. Wei et al. [51] proposed that VRE is directly related to amplitude of the pendulum displacement. Therefore, VRE performance is expected to degrade around resonance frequency of pendulum.
- **Step response of the accelerometer is expected to be overshoot and oscillation free:** Overshoot and oscillation on step response degrades the measurement performance of the accelerometer exposed to shock loads. Overshoot may result in measurement range saturation, which may cause dramatic measurement errors.

5.2 Effects of Readout Circuits on Performance

Readout circuit arrangement of the QFA and effects of it on measurement range are given in detail in Section 0. In fact, the main part of the readout circuit is load resistor, R_L, which is chosen according to desired measurement range and resolution. However, this resistor is also a part of the closed loop block diagram of the accelerometer system, which means it directly affects the dynamic characteristics of the system. Effects of R_L on dynamic characteristics may change dependent on the design of other system components, especially the controller. On the other hand, load capacitor, C_L, may be used with R_L to filter output of the accelerometer, if it is needed. Firstly, the relation between load resistor and sensor dynamic characteristics is investigated. Three different readout circuit configurations are given Table 5.1:

Table 5.1 Readout Circuits Without Capacitor

	RC-1000-A	**RC-350-A**	**RC-50-C**
$\boldsymbol{R_L}$ **[Ω]**	1000	350	50
$\boldsymbol{C_L}$ **[nF]**	0	0	0
Range [g]	>10	>25	>72

The common characteristic of the readout circuits given in Table 5.1 is that they do not include capacitors. Different measurement range values are obtained using various load resistors. Input-output frequency responses, input-pendulum displacement frequency responses and step responses for these readout circuit configurations are given in Figure 5.1, Figure 5.2 and Figure 5.3:

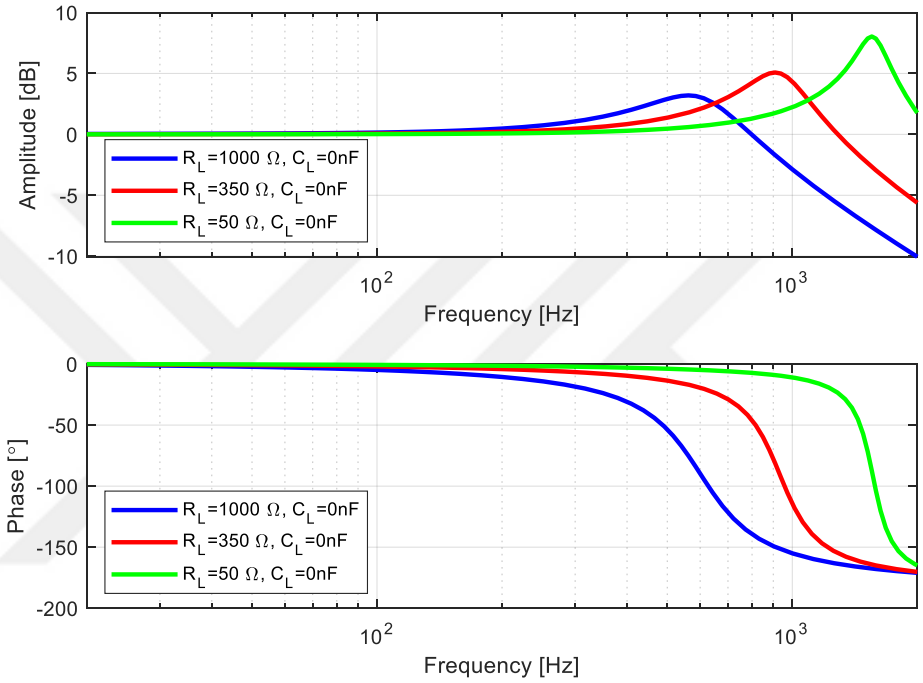

Figure 5.1. Input-Output Frequency Responses of Accelerometers with RC-1000-A, RC-350-A and RC-50-C

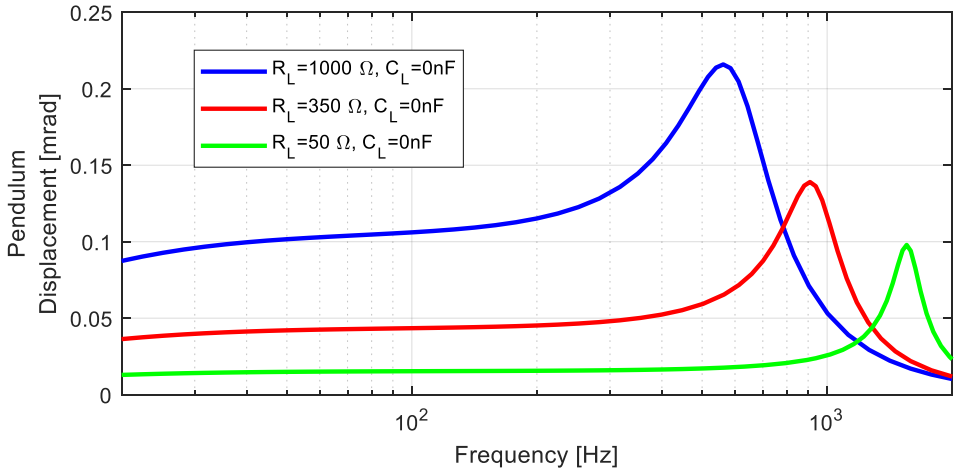

Figure 5.2. Input-Pendulum Displacement Frequency Responses of Accelerometers with RC-1000-A, RC-350-A and RC-50-C

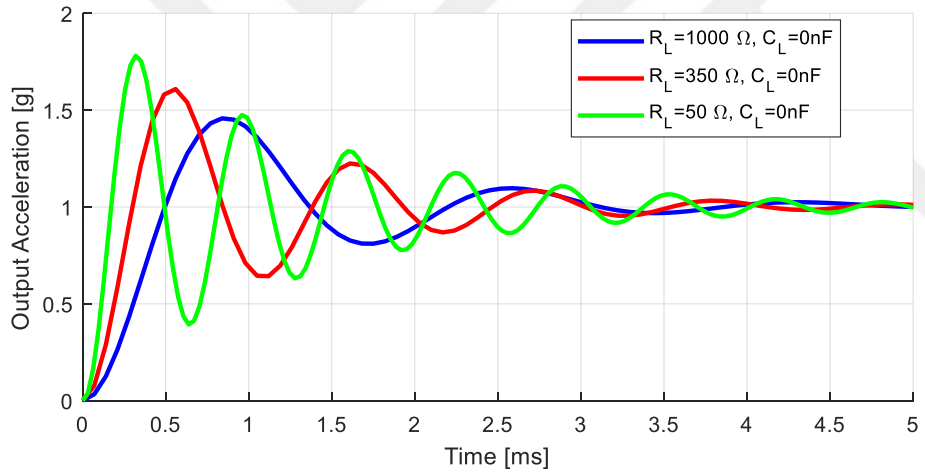

Figure 5.3. Step Responses of Accelerometers with RC-1000-A, RC-350-A and RC-50-C

All three configurations have a resonance as it can be seen in Figure 5.1. As R_L decreases, resonance frequency and amplitude increase. Frequency responses of all configurations are undesired since resonance on output of the accelerometer means excessive measurement around the resonance frequency. Bandwidth more than sufficient frequency may reduce noise performance because of vibration loads. Besides, pendulum displacement has resonance for all the configurations as it is

given in Figure 5.2. As R_L increases, resonance frequency of the pendulum displacement increases but amplitude decreases. On the other hand, amplitude of the pendulum displacement decreases as R_L decreases. This means that as the measurement range increases, the resolution of the output decreases. As it is expected, step responses for all configurations have oscillatory behavior, which can be seen in Figure 5.3.

To obtain better dynamic characteristics, new readout circuits are defined with load capacitors. In Table 5.2, readout circuit configurations with 10g measurement range are defined. Input-output frequency responses, input-pendulum displacement frequency responses and step responses for these readout circuit configurations are given in Figure 5.4, Figure 5.5 and Figure 5.6:

Table 5.2 Readout Circuit Configurations with 10g Measurement Range

	RC-1000-A	**RC-1000-B**	**RC-1000-C**	**RC-1000-D**
$\boldsymbol{R_L}$ **[Ω]**	1000	1000	1000	1000
$\boldsymbol{C_L}$ **[nF]**	0	150	300	450
Range [g]	>10	>10	>10	>10

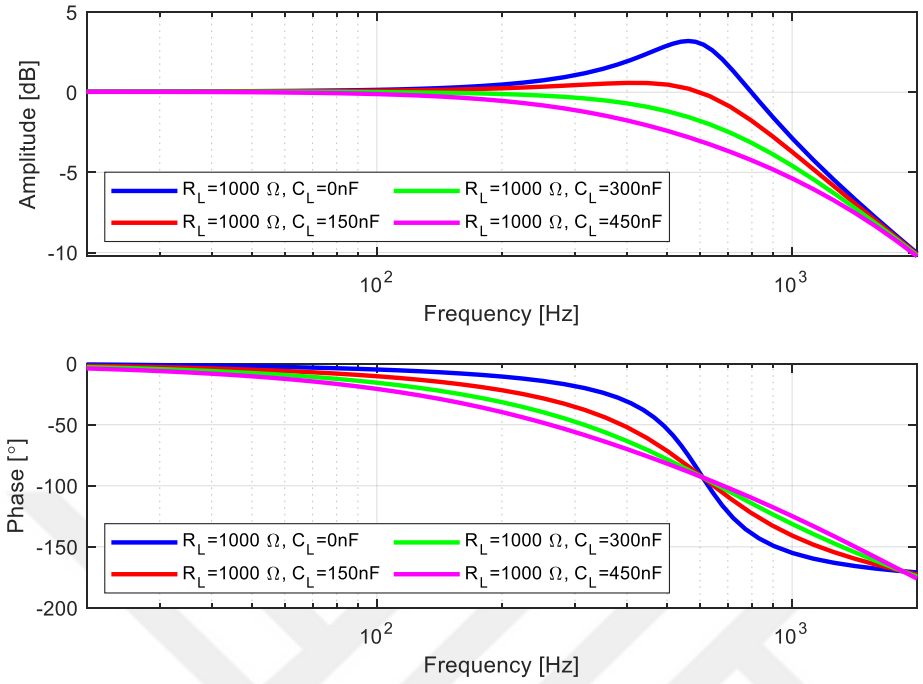

Figure 5.4. Input-Output Frequency Responses of Accelerometers with RC-1000-A, RC-1000-B, RC-1000-C and RC-1000-D

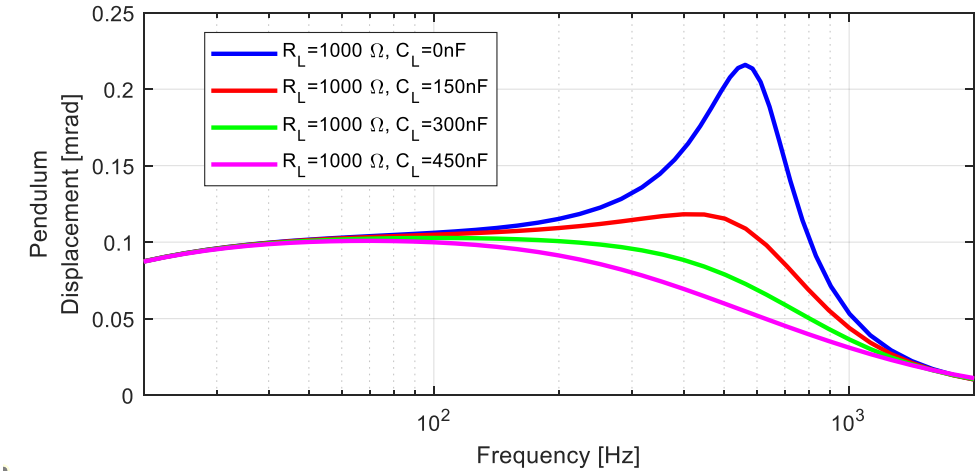

Figure 5.5. Input-Pendulum Displacement Frequency Responses of Accelerometers with RC-1000-A, RC-1000-B, RC-1000-C and RC-1000-D

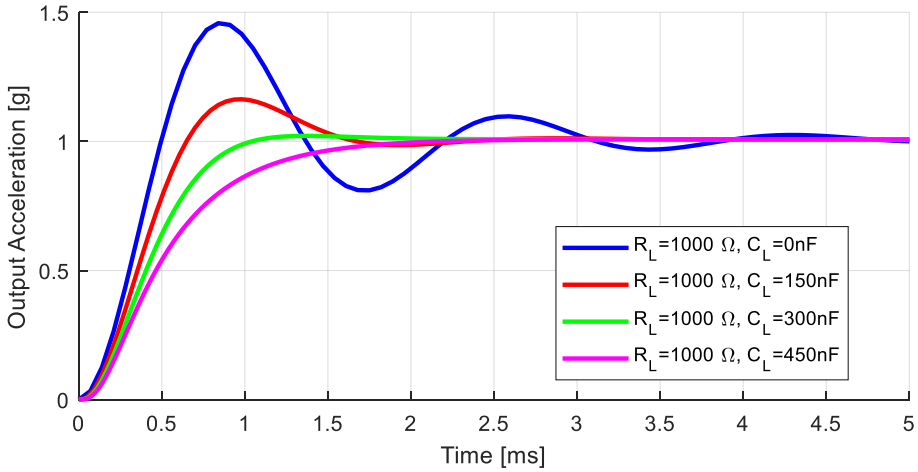

Figure 5.6. Step Responses of Accelerometers with RC-1000-A, RC-1000-B, RC-1000-C and RC-1000-D

As it can be seen in Figure 5.4 and Figure 5.5, capacitor usage in the readout circuit damps the resonance of output and pendulum displacement responses. Accelerometers with RC-1000-C and RC-1000-D configurations have bandwidth values more than 400Hz and there is no resonance on frequency responses. This behavior results in step response without overshooting, which can be seen in Figure 5.6. In Table 5.3, readout circuit configurations with 25g measurement range are defined. Input-output frequency responses, input-pendulum displacement frequency responses and step responses for these readout circuit configurations are given in Figure 5.7, Figure 5.8 and Figure 5.9:

Table 5.3 Readout Circuit Configurations with 25g Measurement Range

	RC-350-A	**RC-350-B**	**RC-350-C**	**RC-350-D**
R_L [Ω]	350	350	350	350
C_L [nF]	0	300	600	1000
Range [g]	>25	>25	>25	>25

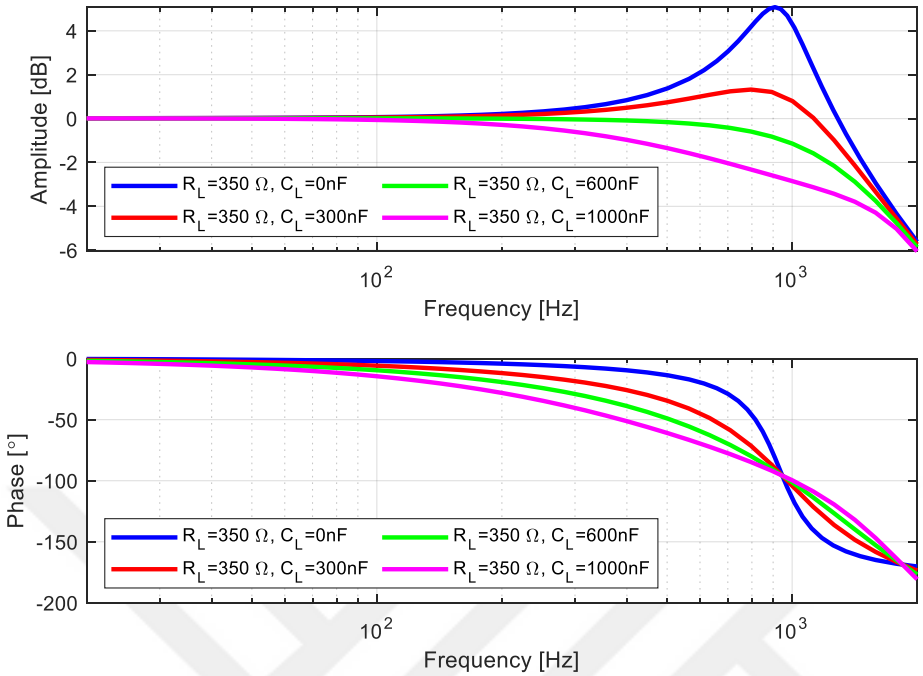

Figure 5.7. Input-Output Frequency Responses of Accelerometers with RC-350-A, RC-350-B, RC-350-C and RC-350-D

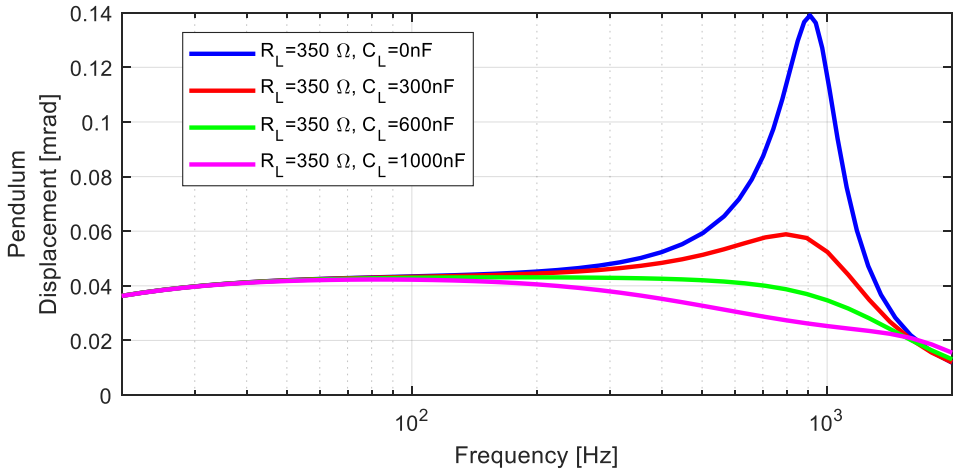

Figure 5.8. Input-Pendulum Displacement Frequency Responses of Accelerometers with RC-350-A, RC-350-B, RC-350-C and RC-350-D

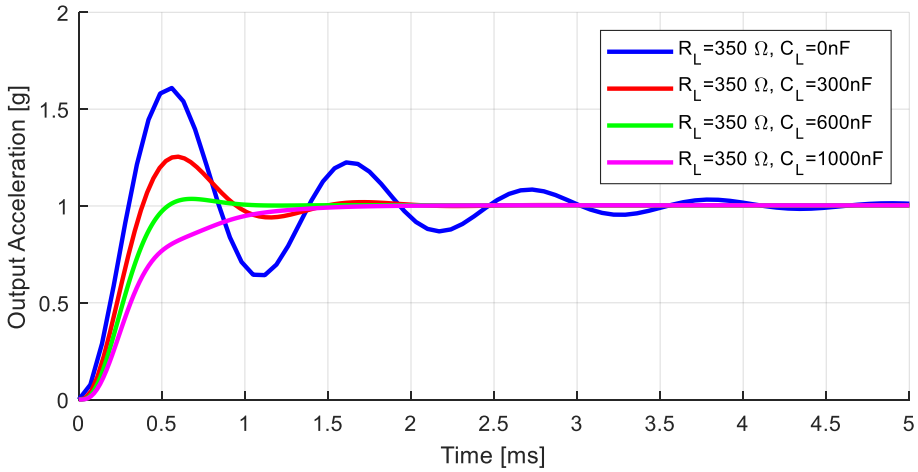

Figure 5.9. Step Responses of Accelerometers with RC-350-A, RC-350-B, RC-350-C and RC-350-D

As it can be seen in Figure 5.7 and Figure 5.8, effects of capacitor usage is same as readout circuits with 10g measurement range. Accelerometers with RC-350-C and RC-350-D configurations have bandwidth values more than 400Hz and there is no resonance on frequency responses. As it is given in Figure 5.9, configuration with RC-350-C has no overshoot and RC-350-D has 3% overshoot only. Lastly, in Table 5.4, readout circuit configurations with 72g measurement range are defined. Input-output frequency responses, input-pendulum displacement frequency responses and step responses for these readout circuit configurations are given in Figure 5.10, Figure 5.11 and Figure 5.12:

Table 5.4 Readout Circuit Configurations with 72g Measurement Range

	RC-50-A	**RC-50-B**	**RC-50-C**	**RC-50-D**
$\boldsymbol{R_L}$ **[Ω]**	50	50	50	50
$\boldsymbol{C_L}$ **[nF]**	0	5000	10000	20000
Range [g]	>72	>72	>72	>72

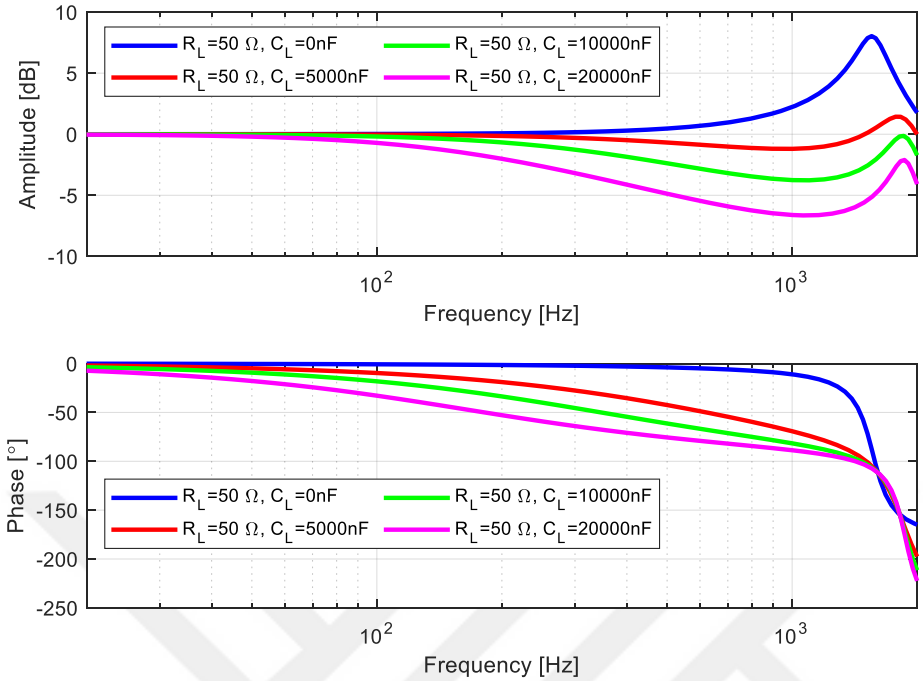

Figure 5.10. Input-Output Frequency Responses of Accelerometers with RC-50-A, RC-50-B, RC-50-C and RC-50-D

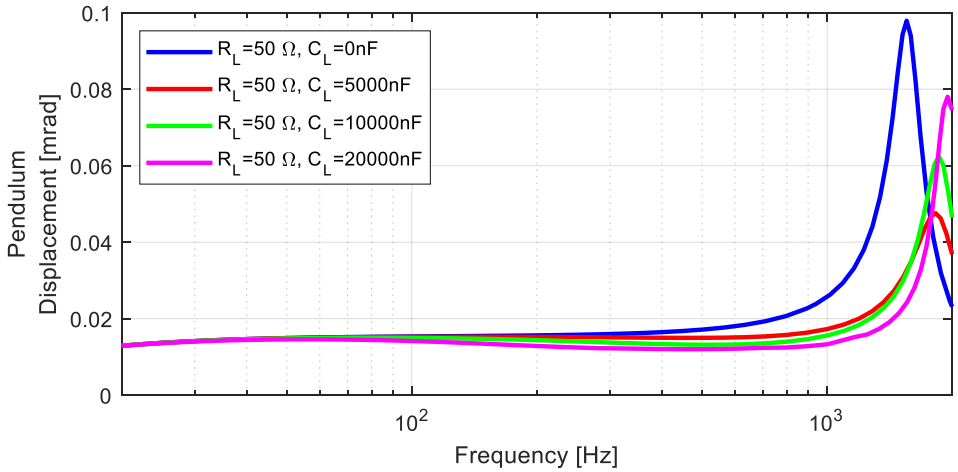

Figure 5.11. Input-Pendulum Displacement Frequency Responses of Accelerometers with RC-50-A, RC-50-B, RC-50-C and RC-50-D

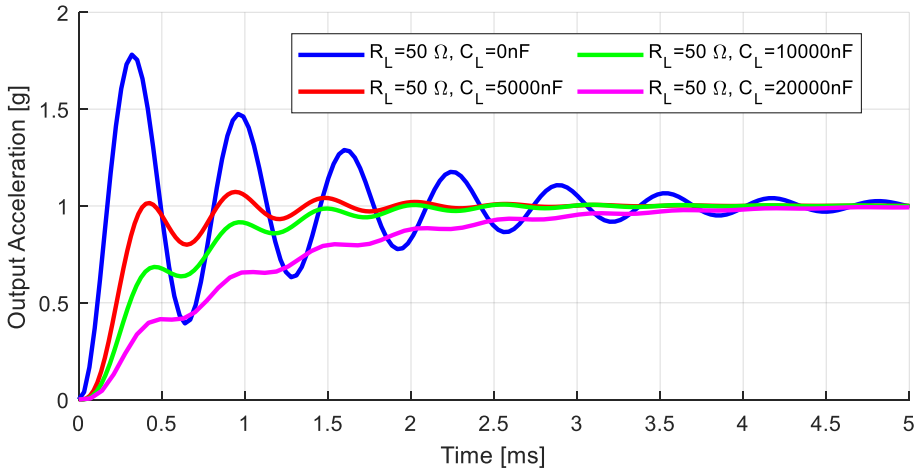

Figure 5.12. Step Responses of Accelerometers with RC-50-A, RC-50-B, RC-50-C and RC-50-D

As it can be seen in Figure 5.10 and Figure 5.11, effects of capacitor usage on output and pendulum frequency responses are not same as 10g and 25g measurement range configurations. Amplitude of the resonance of output frequency response decreases as capacitor value increases. However, capacitor usage also dramatically decreases amplitude of the output frequency response in low frequencies. Resonance of frequency response of pendulum displacement increases with capacitor usage with more than 5000nF. These resonance characteristics cause oscillations on step response of the system even though there is no overshoot for RC-50-C and RC-50-D. Using a capacitor does not suffice for achieving desired dynamic behavior while having a measurement range of 72g. Different design modifications are required for this purpose.

5.3 Effects of Squeeze Film Damping on Performance

In Section 3.3, pendulum in the accelerometer is modelled as a single degree of freedom rotational system and rotational damping coefficient, $C_r(\theta)$, only includes squeeze film effects, is introduced. In this section, the value of rotational damping coefficient is assumed to be three times its actual value. In application, SFD can be increased by decreasing distance between pendulum and magnetic cases (air gap).

Frequency responses and shock responses of the systems with increased SFD and readout circuits RC-1000-A, RC are given in Figure 5.13, Figure 5.14 and Figure 5.15. Results are given for both actual and increased SFD to be able to compare them.

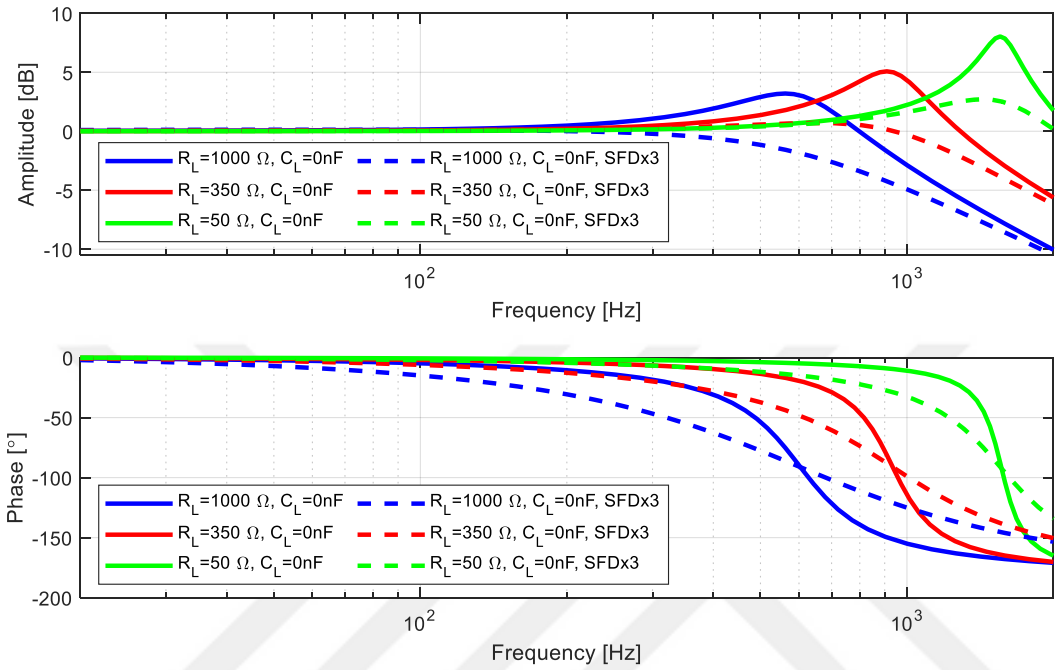

Figure 5.13. Input-Output Frequency Responses of Accelerometers with Actual&Increased SFD and RC-1000-A, RC-350-A and RC-50-C

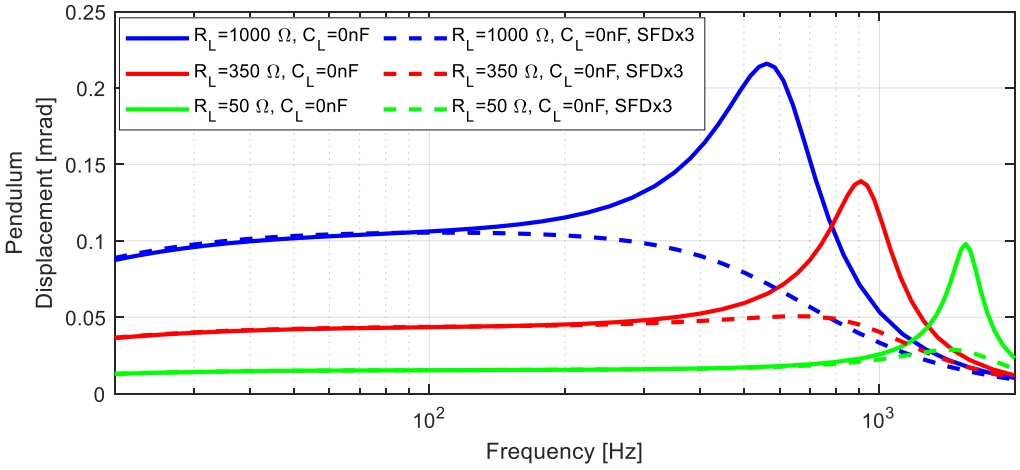

Figure 5.14. Input-Pendulum Displacement Frequency Responses of Accelerometers with Actual&Increased SFD and RC-1000-A, RC-350-A and RC-50-C

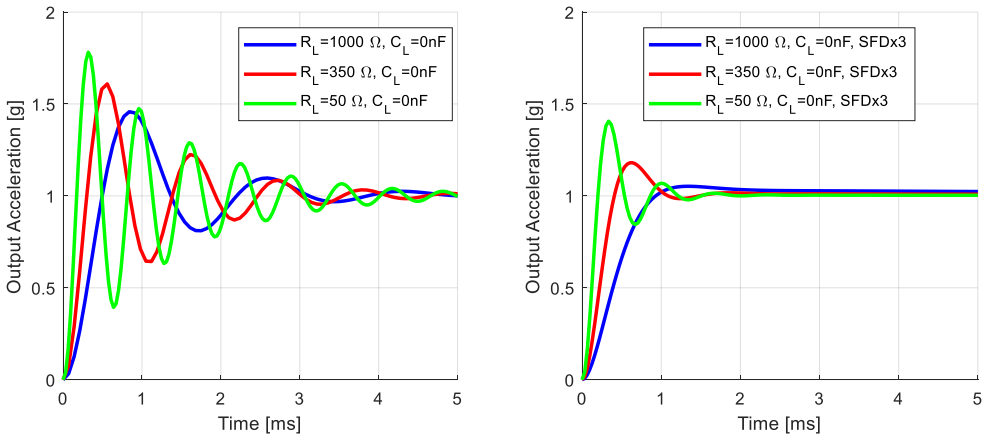

Figure 5.15. Step Responses of Accelerometers with Actual&Increased SFD and RC-1000-A, RC-350-A and RC-50-C

As it is given in Figure 5.13 and Figure 5.14, two times increased SFD dramatically reduces the amplitude of the resonances of output and pendulum displacement frequency responses of the systems. At the same time, it decelerates the phase response of the systems especially below resonance frequencies. As expected, it reduces overshoots and oscillations on the step responses which can be seen in Figure 5.15. However, all configurations still need load capacitors to reach desired dynamic behavior without resonances in frequency responses and overshoots, oscillations on step responses. In Table 5.5, increased SFD and readout circuit configurations with 10g, 25g and 72g measurement ranges are defined. Input-output frequency responses, input-pendulum displacement frequency responses and step responses for these readout circuit configurations are given in Figure 5.16, Figure 5.17 and Figure 5.18:

Table 5.5 Increased SFD&Readout Circuits Configurations with 10g, 25g and 72g Measurement Ranges

	RC-1000-E	**RC-350-E**	**RC-50-E**
$\boldsymbol{R_L}$ **[Ω]**	1000	350	50
$\boldsymbol{C_L}$ **[nF]**	100	1000	10000
Range [g]	>10	>25	>72

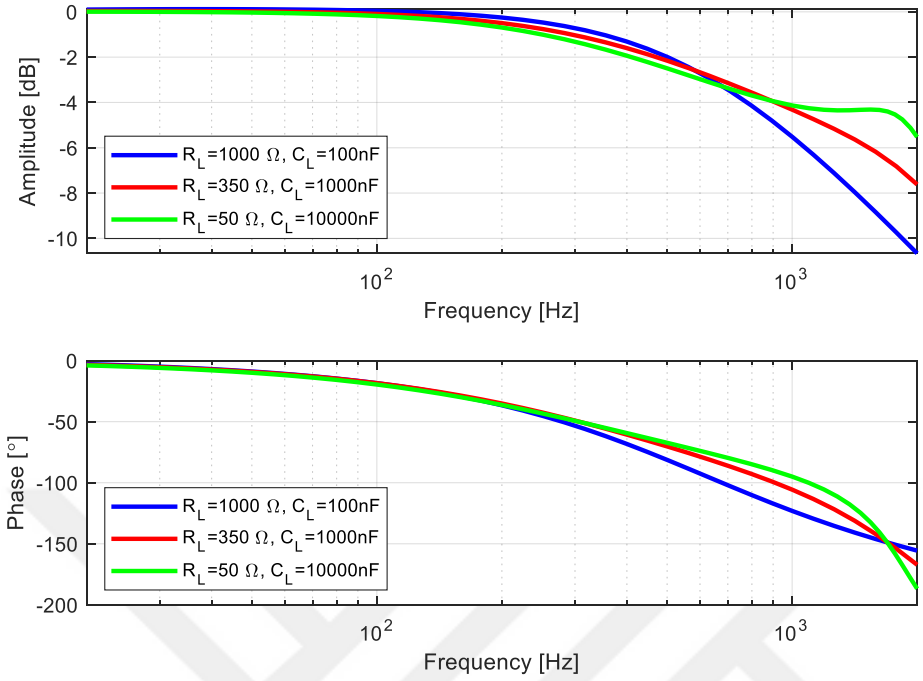

Figure 5.16. Input-Output Frequency Responses of Accelerometers with Increased SFD and RC-1000-E, RC-350-E and RC-50-E

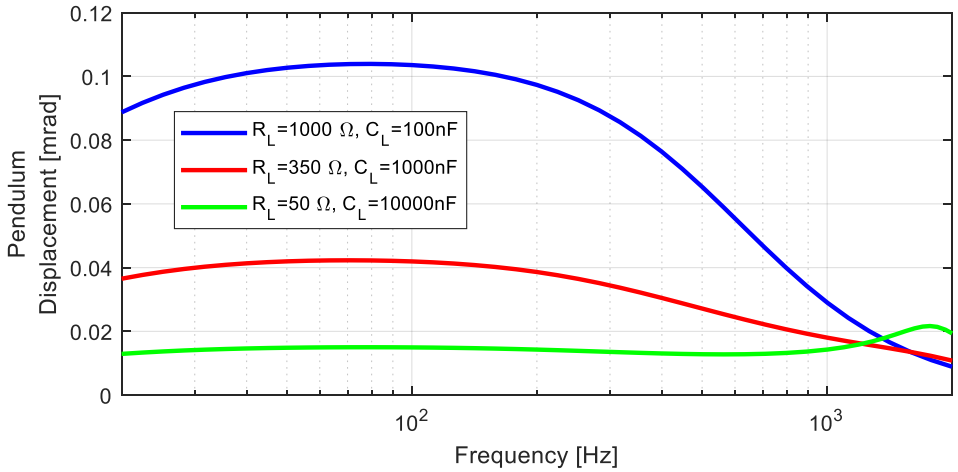

Figure 5.17. Input-Pendulum Displacement Frequency Responses of Accelerometers with Increased SFD and RC-1000-E, RC-350-E and RC-50-E

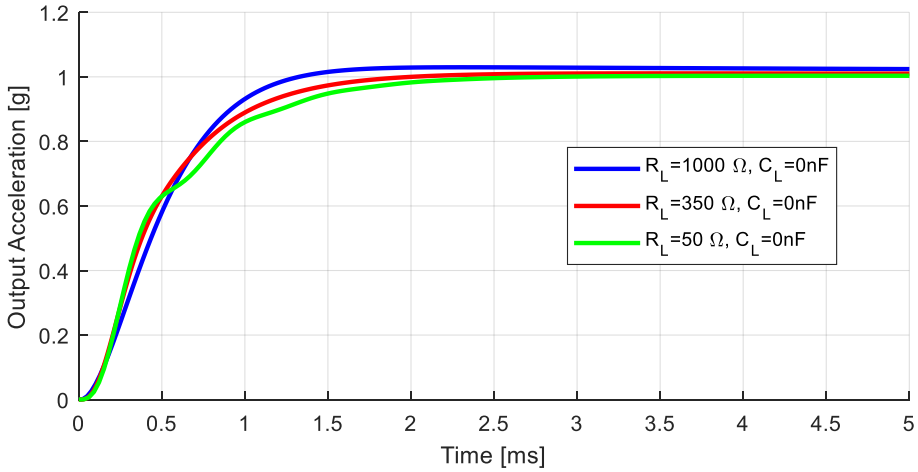

Figure 5.18. Step Responses of Accelerometers with Increased SFD and RC-1000-E, RC-350-E and RC-50-E

As it can be seen in Figure 5.16, Figure 5.17 and Figure 5.18, systems with increased SFD and readout circuits RC-1000-E, RC-350-E and RC-50-E have desired dynamic characteristics. Accelerometers with all these configurations have bandwidth values more than 400Hz, frequency responses without resonances and step responses without overshoots and oscillations. However, it should be noted that increased SFD and load capacitor usage decelerate the system response. To reach dynamic requirements with a faster accelerometer and readout circuit system, controller in the system can be modified. On the other hand, noise and VRE performances of the system must be investigated by experiments for the system with increased SFD.

5.4 Conclusions

In this section, effects of design parameters; R_L, C_L and SFD on dynamic performance of the system are investigated by simulations. Frequency responses and step responses of the closed loop system are observed for each different design configuration. First, dynamic behavior of readout circuit configurations having 10g, 25g and 72g measurement range and without C_L are observed. Output and pendulum displacement frequency responses for all cases have a resonance with high amplitude. To damp these resonances, readout circuits with capacitors are defined

and simulations are repeated. Amplitude of the resonances of output frequency responses decrease as capacitor value increases. Moreover, step responses without overshoot and oscillations are obtained by capacitor usage for configurations with 10g and 25g measurement range. However, capacitor usage dramatically decreases amplitude of the output frequency response in low frequencies, for readout circuits have 72g measurement range. Then, effects of increased SFD on dynamic behavior of the accelerometer are investigated. It can be said that, by increasing SFD two times and using appropriate capacitors, configurations of RC-1000-E, RC-350-E and RC-50-E reach required dynamic performance. All three configurations have frequency responses without resonance and step responses without overshoot and oscillation. Bandwidth values are obtained more than 400Hz and settling times are obtained less than 3ms, which are satisfactory results.

CHAPTER 6

CONCLUSION

6.1 General Conclusion

In this study, all components within the QFA are modeled using analytical, numerical, or experimental methods. Pendulum structure in the system is modelled as a single degree of rotational system. Stiffness and inertia coefficients of the pendulum are modelled by analytical calculations and obtained by CAD software correspondingly. The squeeze film effects on the pendulum are modelled as rotational damping coefficient dependent on pendulum displacement. Moreover, modelling of magnetic feedback torquer, controller and readout circuit are presented. Subsequently, the QFA is modeled as open loop and closed loop systems and the obtained models are validated through verification experiments. For the open loop system, an experimental setup is provided to characterize capacitive pickoff gain of the accelerometer and test open loop test prototype against step inputs with different amplitudes. Simulation and test results for settling times of the step responses indicate a maximum difference of 6% under a 50% displacement ratio. Difference between results increases dramatically for larger displacements. Also, for the closed loop system, an experimental setup including a mechanical shaker is used to obtain frequency response and shock response of the accelerometer. Simulation and test results for frequency responses and shock responses exhibit a maximum difference of 10%. The consistency between verification experiments and model outputs demonstrates the strength and capability of the presented modeling methods and the resulting open loop and closed loop sensor models. Finally, the effects of readout circuit and SFD design parameters on dynamic performance are investigated using the closed loop model. The obtained closed loop model can be utilized for examining sensor dynamic behavior, optimization and in new design studies.

6.2 Recommendations for Future Work

Further studies on the research area may focus to the topics as given below:

- In this study, pendulum is modelled analytically as a single degree of freedom rotational system. Therefore, model of pendulum includes only the first bending mode of the system. Pendulum may be modelled again to include higher order vibrational modes. Modelling with state-space method can be used for that purpose.
- Transient response of the sensor under random vibrational loads can be investigated. Damping model can be revised/optimized for further studies to improve the accuracy of the model for random vibrational inputs.
- Effects of mechanical, electronical and assembling tolerances on performance can be investigated by sensitivity analysis.
- SFD in the system can be investigated for different gasses by analysis and through experiments.
- VRE performance of the accelerometer can be investigated by simulations and experiments. First, the relation between VRE and frequency responses of the system can be obtained by a series of sine sweep and VRE tests. Some asymmetries can be added to the closed loop model of the system, such as uneven air gap distances to investigate effects of asymmetries in the system on VRE by simulations.

REFERENCES

[1] Groves, P.: Principles of GNSS, Inertial and Multisensor Integrated Navigation Systems, Second Edition, (2013)

[2] Tazartes, D.: An historical perspective on inertial navigation systems. In: 2014 International Symposium on Inertial Sensors and Systems (INERTIAL), pp. 1–5 (2014). https://doi.org/10.1109/ISISS.2014.6782505

[3] Lawrence, A.: Modern Inertial Technology: Navigation, Guidance and Control. Mechanical Engineering Series. Springer (2001).

https://books.google.com.tr/books?id=Sjl1qfyaBWcC

[4] Grewal, M., Weill, L. andrews, A.: Global Positioning Systems, Inertial Navigation and Integration, Second Edition, (2007).

https://doi.org/10.1002/9780470099728.ch3

[5] Prosser, S.J.: Aerospace sensor systems and applications. Measurement Science and Technology 9(1), 023 (1998) https://doi.org/10.1088/0957-0233/9/1/023

[6] El-Sheimy, N., Youssef, A.: Inertial sensors technologies for navigation applications: state of the art and future trends. Satellite Navigation 1, 2 (2020) https://doi.org/10.1186/s43020-019-0001-5

[7] Passaro, V., Cuccovillo, A., Vaiani, L., De Carlo, M., Campanella, C.E.: Gyroscope technology and applications: A review in the industrial perspective. Sensors 17, 2284 (2017) https://doi.org/10.3390/s17102284

[8] Fenercioğlu, T.O., Yalçinkaya, T.: Computational–experimental design framework for laser path length controller. Sensors 21(15) (2021) https://doi.org/10.3390/s21155209

[9] Kahveci, Gençoğlu, C., Yalçinkaya, T.: Experimental analysis and multiscale modeling of the dynamics of a fiber-optic coil. Sensors 22(2) (2022) https://doi.org/10.3390/s22020582

[10] Remillieux, G., Delhaye, F.: Sagem coriolis vibrating gyros: A vision realized. In: 2014 DGON Inertial Sensors and Systems (ISS), pp. 1–13 (2014). https://doi.org/10.1109/InertialSensors.2014.7049409

[11] Delhaye, F.: Hrg by safran: The game-changing technology. In: 2018 IEEE Inter-national Symposium on Inertial Sensors and Systems (INERTIAL), pp. 1–41 (2018). https://doi.org/10.1109/ISISS.2018.8358163

[12] Titterton, D., Weston, J.L., Electrical Engineers, I., Aeronautics, A.I., Astronautics: Strapdown Inertial Navigation Technology. IEE Radar Series. Institution of Engineering and Technology (2004).

https://books.google.com.tr/books?id=WwrCrn54n5cC

[13] Jacobs, E.D.: Accelerometer. US3702073A, November 1972. https://patents.google.com/patent/US3702073A/en

[14] Bao, M., Yang, H.: Squeeze film air damping in mems. Sensors and Actuators A: Physical 136(1), 3–27 (2007) https://doi.org/10.1016/j.sna.2007.01.008 . 25th Anniversary of Sensors and Actuators A: Physical

[15] Pratap, R., Mohite, S., Pandey, A.: Squeeze film effects in mems devices. Journal of the Indian Institute of Science 87 (2007)

[16] Bao, M., Yang, H., Sun, Y., French, P.J.: Modified reynolds' equation and analytical analysis of squeeze-film air damping of perforated structures. Journal of Micromechanics and Microengineering 13(6), 795 (2003)

https://doi.org/10.1088/0960-1317/13/6/301

[17] Pagnotta, L., Pantano, M., Nigro, S.: Analytical and numerical modeling of squeeze-film damping in perforated microstructures. Microfluidics and Nanofluidics 12, 971–979 (2012) https://doi.org/10.1007/s10404-011-0931-1

[18] Pandey, A., Pratap, R.: A comparative study of analytical squeeze film damping models in rigid rectangular perforated mems structures with experimental results.

Microfluidics and Nanofluidics 4, 205–218 (2007) https://doi.org/10.1007/s10404-007-0165-4

[19] Pandey, A.K., Pratap, R., Chau, F.S.: Analytical solution of the modified reynolds equation for squeeze film damping in perforated mems structures. Sensors and Actuators A: Physical 135(2), 839–848 (2007) https://doi.org/10.1016/j.sna.2006.09.006

[20] Pasquale, G.D., Veijola, T., Som`a, A.: Modelling and validation of air damping in perforated gold and silicon mems plates. Journal of Micromechanics and Microengineering 20(1), 015010 (2009) https://doi.org/10.1088/0960-1317/20/1/015010

[21] Pasquale, G.D., Veijola, T., Som`a, A.: Modelling and validation of air damping in perforated gold and silicon mems plates. Journal of Micromechanics and Microengineering 20(1), 015010 (2009) https://doi.org/10.1088/0960-1317/20/1/0150102

[22] Pandey, A.K., Pratap, R.: Coupled nonlinear effects of surface roughness and rarefaction on squeeze film damping in mems structures. Journal of Micromechanics and Microengineering 14(10), 1430 (2004) https://doi.org/10.1088/0960-1317/14/10/020

[23] Pagnotta, L., Pagnotta, M., Nigro, S.: A numerical study of squeeze-film damping in mems-based structures including rarefaction effects. Frattura ed Integrit`a Strutturale 23, 103–113 (2013) https://doi.org/10.3221/IGF-ESIS.23.11

[24] Veijola, T.: Analytic damping model for an mem perforation cell. Microfluidics and Nanofluidics 2, 249–260 (2006) https://doi.org/10.1007/s10404-005-0072-5

[25] Li, C., Zhang, D., Cheng, G., Zhu, Y.: Microelectromechanical systems for nanomechanical testing: Electrostatic actuation and capacitive sensing for high-strain-rate testing. Experimental Mechanics 60(3) https://doi.org/10.1007/s11340-019-00565-5

[26] Langlois, W.E.: Isothermal squeeze films. Quarterly of Applied Mathematics 20(2), 131–150 (1962). Accessed 2023-12-05

[27] Chen, S., Feng, Z.: Damping and stiffening forces of a squeeze film between two plates. Nonlinear Dynamics 87, 1–10 (2017) https://doi.org/10.1007/s11071-016-3150-1

[28] LANGLOIS, W.E.: Isothermal squeeze films. Quarterly of Applied Mathematics 20(2), 131–150 (1962). Accessed 2023-12-05

[29] Starr, J.B.: Squeeze-film damping in solid-state accelerometers. IEEE 4th Technical Digest on Solid-State Sensor and Actuator Workshop, 44–47 (1990)

[30] Veijola, T., Ruokonen, K., Tittonen, I.: Compact model for the squeezed-film damping including the open border eects. 2001 International Conference on Modeling and Simulation of Microsystems - MSM 2001 (2001)

[31] Veijola, T.: End effects of rare gas flow in short channels and in squeezed-film dampers. 2001 International Conference on Modeling and Simulation of Microsystems - MSM 2001, 104–107 (2002)

[32] Veijola, T., Pursula, A., R̊aback, P.: Extending the validity of squeezed-film damper models with elongations of surface dimensions. Journal of Micromechanics and Microengineering - J MICROMECHANIC MICROENGINEER 15 (2005) https://doi.org/10.1088/0960-1317/15/9/003

[33] Xu, X., Fang, W., Bai, J., Chen, J., Yao, Y., Lu, Q.: Extending the validity of squeeze film damping models with lower aspect ratios. Sensors 22(3) (2022) https://doi.org/10.3390/s220310543

[34] Fedder, G.K., Mukherjee, T., Vemuri, S.C.: Low-order squeeze film model for simulation of mems devices. (2000).

https://api.semanticscholar.org/CorpusID:35888733

[35] Qianbo, l., Fang, W., Wang, C., Bai, J., Yao, Y., Chen, J., Xu, X., Huang, W.: Investigation of a complete squeeze-film damping model for mems devices. Microsystems Nanoengineering 7, 54 (2021) https://doi.org/10.1038/s41378-021-00279-6

[36] Moeenfard, H.: Analytical modeling of squeeze film damping in dual axis torsion microactuators. Surface Review and Letters 22 (2015) https://doi.org/10.1142/S0218625X15500067

[37] Younis, M., Nayfeh, A.: Simulation of squeeze-film damping of microplates actuated by large electrostatic load. Journal of Computational and Nonlinear Dynamics - J COMPUT NONLINEAR DYN 2 (2007)

https://doi.org/10.1115/1.2727491

[38] Erdener Ö (2005) Mems accelerometer design, Dissertation, İstanbul Technical University

[39] Chen, C.-S., Kuo, W.-J.: Squeeze and viscous dampings in micro electrostatic comb drives. Sensors and Actuators A: Physical 107(2), 193–203 (2003) https://doi.org/10.1016/S0924-4247(03)00295-4

[40] Sun, D., Chen, W., Dong, W., Guo, W., Liu, C., Wang, G., Yan, X., Xu, B.: Squeeze film damping effect on switching time of a moems optical switch. Optik 115(8), 380–384 (2004) https://doi.org/10.1078/0030-4026-00384

[41] Mo, Y., Du, L.M., Qu, B., Peng, B., Yang, J.: Squeeze film air damping ratio analysis of a silicon capacitive micromechanical accelerometer. Microsystem Technologies 24, 1089–1095 (2017)

[42] Jallouli, A., Kacem, N., Najar, F., Bourbon, G., Joseph, L.: Modeling and experimental characterization of squeeze film effects in nonlinear capacitive circular microplates. Mechanical Systems and Signal Processing 127, 68–88 (2019) https://doi.org/10.1016/j.ymssp.2019.02.060

[43] IEEE Standard Specification Format Guide and Test Procedure for Linear Single-Axis, Nongyroscopic Accelerometers. (2018)

[44] Beer, F., Jr. Johnston, E.R., DeWolf, J., Mazurek, D.: Mechanics of Materials. McGraw-Hill Education, (2011).

[45] CFD Module User's Guide, COMSOL Multiphysics® v. 6.0. COMSOL AB, Stockholm, Sweden. 2023

[46] Wang, C., Li, X., Kou, K., Long, C.: Optimization of magnetic hat for quartz flexible accelerometer. Sensor Review 36, 71–76 (2016)
https://doi.org/10.1108/SR-04-2015-0067

[47] Özmen, B., Şahin, M., Özgen, G.O.: Kuvars Sarkaçli Ivmeölçer Ve Okuma Devresi Sistem Dinamiğinin Karakterizasyonu. In: 10. Savunma Teknolojileri Kongresi (SAVTEK) (2022)

[48] MathWorks®, MATLAB®: Primer, (R2018a), Natick, Massachusetts, USA. 2023

[49] MathWorks®, SIMULINK®: User's Guide, (R2019b), Natick, Massachusetts, USA. 2023

[50] Environmental Engineering Considerations and Laboratory Tests. (2008)

[51] Wei, Y., Yang, J., Li, P., Zhang, X., Liang, P.: Analysis and optimization method of the vibration rectification error of a pendulous accelerometer. IEEE Sensors Journal 21(18), 19847–19856 (2021)
https://doi.org/10.1109/JSEN.2021.30975855